

27 Modeling of Nanostructures

Hande Toffoli¹ · Sakir Erkoç¹ · Daniele Toffoli²

¹Department of Physics, Middle East Technical University, Ankara, Turkey

²Department of Chemistry, Middle East Technical University, Ankara, Turkey

Introduction	996
Hierarchy of Methods	996
0D Structures: Nanoparticles	996
Global Optimization with Empirical Potentials	999
Local Optimization with Higher Accuracy Methods	1001
1D Structures: Nanotubes, Nanowires, Nanorods	1009
Elastic and Structural Properties	1010
Structural Properties	1013
Electronic, Magnetic and Optical Properties	1014
2D Structures: Graphene and Derivatives	1017
Graphene, Nanosheets, Nanoribbons, Nanobelts, Nanostrips	1019
Electronic and Mechanical Properties	1024
Magnetic and Optical Properties	1032
Adsorption Phenomena	1035
References	1036

Abstract: Materials properties show a dependence on the dimensionality of the systems studied. Due to the increased importance of surfaces and edges, lower-dimensional systems display behavior that may be widely different from their bulk counterparts. As a means to complement the newly developed experimental methods to study these reduced dimensional systems, a large fraction of the theoretical effort in the field continues to be channeled towards computer simulations. This chapter reviews briefly the computational methods used for the low dimensional materials and presents how the materials properties change with dimensionality. Low dimensional systems investigated are classified into a few broad classes: 0D nanoparticles, 1D nanotubes, nanowires, nanorods, and 2D graphene and derivatives. A comprehensive literature will guide the readers' interest in computational materials sciences.

Introduction

Hierarchy of Methods

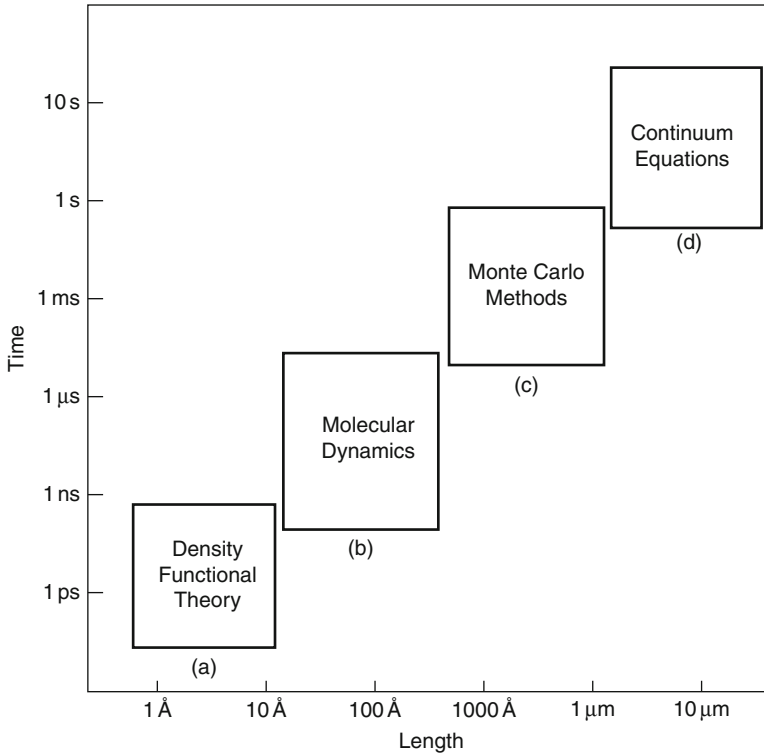
Methods for materials modeling are based on the particular length and time scales used for the investigation of various materials properties that operate only over those scales. This has led to basically four independent methodological streams, which may be categorized as ab-initio density functional theory, molecular dynamics, statistical methods based on Monte Carlo algorithms, and continuum mechanics (see  Fig. 27-1 for the ranges of them). Each of these is computationally intensive within its own range. However, the expanding capabilities of computational methods due to the increasing power of computers and continuing development of efficient algorithms, together with advances in the synthesis, analysis, and visualization of materials at increasingly finer spatial and temporal resolutions, have spawned a huge effort in the modeling of materials phenomena.

Since the materials properties are directly related with the dimensionality of materials, particularly at the nanoscale, it would be better to classify the methods of modeling of nanostructures with respect to the dimensionality, such as zero-dimensional (0D), one-dimensional (1D), two-dimensional (2D), and three-dimensional (3D) materials. At the nanoscale the first three dimensionalities (0D, 1D, 2D) are commonly used, but the 3D materials are usually considered as macroscopic systems; therefore those materials are not the subject of this chapter.

0D Structures: Nanoparticles

The class of nanomaterials that may be termed *zero-dimensional* comprise systems that are confined within up to several hundreds of nanometers in all three dimensions. Although there exists no clear-cut size threshold at which a system switches from a zero-dimensional system to bulk, there is a rather well-defined class of systems that fit the above definition with unique and intriguing properties. The most commonly studied zero-dimensional systems are *quantum dots*, *nanoparticles* (or *clusters*), and *cage-like structures*. In this section, we shall begin with an overview of methods used to study such materials.

After the 1980s, the field of nanoparticles has seen increasing activity. The results of these studies and their applications have been collected in several reviews (Balasubramanian 1990; Baletto and Ferrando 2005; Bonacic-Koutecky et al. 1991; Brack 1993; de Heer 1993; Halicioglu



■ Fig. 27-1

Ranges of scales used for different methods in materials properties (Adapted from Vvedensky 2004)

and Bauschlicher 1988; Morse 1986; Ustunel and Erkoç 2007; Weltner and Van Zee 1984). Studies on clusters have been concentrated on such diverse applications as catalysis, chemisorption and substrate adsorption, laser applications, magnetism, nucleation, photographic processes, and reactivity.

The term *cluster* may, in the broadest sense, be defined as an aggregate of atoms or molecules that form a size regime between molecules and bulk materials. It is far from a straightforward task to define the range of number of atoms which constitute a cluster. In contrast to their bulk counterparts, structural and electronic properties of clusters display a rather strong dependence on size and geometric configuration due to their large surface-to-volume ratio. Thus in order to understand the properties of clusters a careful determination of the equilibrium structure is crucial. In general, the equilibrium geometry is determined by locating the global minimum of the *potential energy surface* (PES) of a cluster, which in principle can be mapped out by calculating the total energy as a function of all possible locations of the atoms. Unfortunately even the smallest clusters often have extremely complicated potential energy surfaces with practically countless local minima. This requires a thorough search over the entire PES for a realistic determination of the equilibrium structure.

An added complication to the difficulty of determining the global minima is that clusters with different but similar sizes of the same material may present PESs that are entirely different. It is likely then that the equilibrium shape of a cluster of a given material and size is

significantly different from a different size cluster of the same material. Fortunately, some similarities may be found in the vast number of possible structures. Mass spectroscopy of clusters reveal that certain sizes of clusters are preferred over others, indicated by the high abundance detected (Martin 1996). The number of atoms or molecules in a preferred cluster is commonly referred to as a *magic number*. The origin of a magic number may be the completion of a *geometric* or an *electronic* shell of the cluster. The particular geometric or electronic shell being completed obviously depends upon the constituents of the clusters and the bonding between them. For instance, noble gases are found in polyhedral form whereas metallic clusters prefer cubic or prolate structures (Johnston 2002). The search for magic numbers has been the subject of a very large number of works (Anagnostatos 1987; Balasubramanian 1990; Bonacic-Koutecky et al. 1991; Haberland 1994; Jarrold and Constant 1991; Moraga 1993; Yang et al. 2006).

In order to map out the energy landscape of nanoparticles an adequate model for the interatomic interactions within the cluster needs to be employed. Empirical potentials, the tight-binding approximation, and density-functional theory whose brief description has been given in previous sections are the most commonly used methods in literature. While empirical potentials (Erkoc 1997, 2001) offer an efficient means of exploring the PES and determining the equilibrium structure of large clusters, calculations based on the tight-binding approximation and density functional theory are preferred for more accurate and detailed description of geometrical and electronic properties of small to medium sized clusters.

Once the method of choice is determined for interatomic interactions, the corresponding potential energy surface may be explored using *global search algorithms* to determine the lowest lying minima. A concise review of global optimization methods are given in the reviews (Baletto and Ferrando 2005; Dugan and Erkoc 2009; Wales and Doye 1997). Here, we shall briefly describe a few of them.

The basin hopping algorithm (Wales and Doye 1997) belongs to a class of optimization methods called *hypersurface deformation methods*. These methods aim to simplify the PES by applying a map that smooths it out. The global minimum of the simplified PES is then mapped back to that of the real PES assuming that it leads back to the global minimum of the real PES. In the basin hopping algorithm, the original, complicated PES, $U(\vec{r})$, is transformed onto a step-like function $\tilde{U}(\vec{r})$ according to the rule (Baletto and Ferrando 2005; Wales and Doye 1997)

$$\tilde{U}(\vec{r}) = \min[U(\vec{r})], \quad (27.1)$$

where the min function implies that a local minimization is to be applied such as the conjugate gradients algorithm (Hestenes and Stiefel 1952).

In many of the cluster applications using basin hopping (Bromley and Flikkema 2005; Doye and Wales 1999; Hsu and Lai 2006; Wales and Doye 1997), this transformed PES is sampled with a Monte Carlo algorithm, sometimes with a fixed acceptance (Wales and Doye 1997).

The second method we shall mention is *the simulated annealing method* (Kirkpatrick et al. 1983), in which the system is evolved at high temperature and then gradually cooled down. Assuming that the system does not get trapped in a basin of attraction which is not the minimum, it reaches the state of lowest energy during the cooling process. Attempts to use simulated annealing to find the global energy minimum in larger systems is frustrated by high-energy barriers that trap the system in metastable configurations (Ma and Wang 2006).

Finally, we briefly describe a class of algorithms that has recently gained popularity, namely, *genetic algorithms*. Genetic algorithms (GAs) are based on ideas borrowed from natural evolution. As explained in Darby and coworkers (2002), they employ operators that are analogues of

the evolutionary processes of genetic crossover, mutation, and natural selection. A GA can be applied to any problem where the variables to be optimized can be encoded to form a string, each string representing a trial solution to the system. In cluster terminology each *string* is a list of coordinates of a cluster. An initial number of clusters are chosen according to some generation scheme (usually random) and locally minimized.

After the creation of the initial generation of strings, each member of this generation is assigned a *fitness parameter* based on a fitness function. In Darby and coworkers (2002), for example, this function was chosen to be the negative exponent of the deviation of the total energy of each cluster from the cluster with minimum energy.

Once a fitness parameter is assigned to each member of the population, a new generation is created: Two *parents* are chosen from members with high fitness parameter for each *offspring* (member of the new generation) and then subjected to the *crossover* operation. A crossover operation for clusters consists of a particular rearrangement and combination of the atomic coordinates in the parent clusters. For an example, see Darby and coworkers (2002). After each new cluster is generated a local minimization is performed. Mating continues in this way until the desired number of offsprings are generated. New fitness parameters are assigned to each offspring. In order to maintain diversity, new genetic material is introduced into the population by means of the *mutation* operator. After mutation in a cluster population, clusters are once again locally minimized.

Finally the next generation is completed by applying *natural selection*. The previous generation and the new generation are ranked in order of fitness and the best N individuals (clusters) are chosen, where N is the population of the original population. These N individuals constitute the new generation, and mating is performed again.

The process of mating, mutation, and selection is repeated for a predetermined number of generations or until a given criterion is reached. This criterion could be, for example, the convergence of the highest fitness to a plateau so that consecutive generations do not produce better results.

Other global search algorithms include parallel random tunneling, conformational space annealing, greedy search method, simulated annealing, quantum annealing, smoothing and hypersurface deformation techniques, lattice methods, growth sequence analysis, and replica exchange method.

Global Optimization with Empirical Potentials

In spite of the wealth of information they provide, global search algorithms ordinarily fail to identify all the minima of a given cluster. The best explored potential surface for clusters belong to possibly the simplest empirical potential, namely, the Lennard-Jones potential. The Lennard-Jones potential is a simple model that captures the long- and short-range behavior of atoms and molecules. It was proposed in 1931 by J. E. Lennard-Jones (1931) and has been used in innumerable studies ever since. It has the following simple form

$$V(r) = 4\epsilon \left[\left(\frac{\sigma}{r} \right)^{12} - \left(\frac{\sigma}{r} \right)^6 \right], \quad (27.2)$$

where ϵ and σ are parameters that determine the depth and the width of the potential well, respectively, and r is the interatomic distance between atom pairs.

The four known structural forms for the LJ potential are (Hartke 2002) as seen in **Fig. 27-2**:

1. Icosahedral: formed by starting from the pentagonal bipyramid and adding a further layer of atoms.
2. Decahedral: icosahedral core surrounded by fcc stacks.
3. Tetrahedral: tetrahedron of atoms in the innermost core.
4. Face-centered cubic : sections of the fcc bulk structure.

For $N < 1,000$, Lennard-Jones clusters follow an icosahedral pattern growth with magic numbers corresponding to *Mackay icosahedra* (Mackay 1962) for $N = 13, 55, 147, 309$, etc. In between these magic numbers, most of the structures are Mackay-like with incomplete outer layers. Exceptions occur when there are alternative structures with complete shells. These are mostly Marks decahedra (Doye 2003) but there are instances of an fcc truncated octahedron and a Leary tetrahedron (Noya and Doye 2006). The preference for icosahedral structures of Lennard-Jones clusters at small sizes is thought to be due to a trade-off between optimal bond distance and strain (Hartke 2002; Krainyukova 2006).

In spite of its simplicity, the Lennard-Jones potential may not be used for accurate description of cluster properties with the possible exception of noble gas clusters. Often empirical potentials that involve a larger number of parameters than the two-parameter Lennard-Jones potential are employed for structural determination.

To understand their behavior at finite temperature, Wu and coworkers studied Zn clusters using the Gupta potential by means of molecular dynamics (Wu et al. 2005). Zn clusters are found to display peculiar structures that are very different from other *sp*-type metal clusters. The $N = 13$ cluster, for instance, has a disordered structure instead of the icosahedral structure found in most metals of the same size. The C_v curve also differs in that it has a double

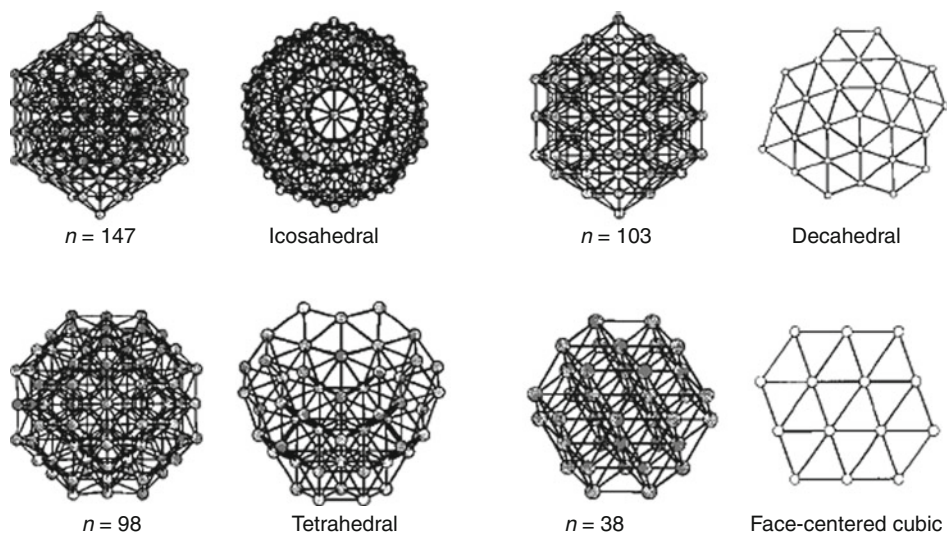


Fig. 27-2

The four basic structures of Lennard-Jones clusters (Reprinted with permission from Hartke (2002). © (2002) by Wiley-VCH Verlag GmbH & Co. KGaA)

peak structure, whereas icosahedral structures display a single peak. The ΔE_2 study in Wu et al. (2005) reveals that magic structures are found at $N = 6, 13, 29, 33, 36, 42, 49,$ and 53 .

In a study by Rey and coworkers (1993), several transition metal clusters (Ni, Pd, Au, and Ag) were studied using different model potentials. Three different *embedded atom models* (EAM) and two different parameterizations of an N-body analytical potential were considered. For Ni clusters, although the binding energies provided by the various models showed differences, the peak stability was obtained for all the models at $N = 13$ (icosahedron) and $N = 19$ (double icosahedron). In this work (Rey et al. 1993), earlier experiments on large Ni clusters ($N = 49$ – 2300) are also quoted where icosahedral growth was observed. For Ni the EAM that was fitted to bulk values (EAM1) gave poorer results than the one fitted to diatomic values. For Pd, Au, and Ag, only EAM1 and one of parameterizations of the analytical potential (TBM1) were compared. EAM1 failed to yield enhanced stability for $N = 13$ and $N = 19$, while TBM1 mostly gave icosahedral structures for both sizes. This shows the importance of parameterization for the accuracy of the model potentials.

In a recent study by Doye (2006), results for Pb clusters were calculated and compared for the Gupta potential and a glue potential in combination with a basin-hopping algorithm. Within the Gupta potential framework, Pb clusters, in contrast to Si, Ge, and Sn, do not show any tendency to form prolate or oblate structures. Their structures are mostly spherical with decahedra being the most favored structure followed by close-packed. This study also presents an interesting comparison between the Gupta potential and the glue potential, which reveals that there is virtually no agreement between the two potentials neither in the magic numbers nor in the resulting structures. This sharp discrepancy demonstrates that one should be very careful while comparing results from different methods. More disordered structures are favored for the glue potential than the Gupta potential because the embedding term dominates for the latter.

An interesting result from the work of Doye (2006) is that for the Gupta potential the uncentered Mackay icosahedron with $N = 54$ is more stable than the complete $N = 55$ Mackay icosahedron. This is because of the strain applied by the external atoms on the center, making it unfavorable to be occupied.

As a final remark on empirical potentials, we note that the particular parameterization of the potential plays a crucial role in correctly identifying structural properties, and caution should therefore be used in interpreting results for empirical potentials. For instance, according to (Michaelian et al. 1999), the global minima of Au clusters are difficult to localize because of the short range of the Au potential. As the range of a potential decreases, the number of global minima associated with the potential increases. As a result of this, different studies have identified different global minima for Au clusters. In addition different potential models for the metal yield different ordering of the lowest lying minima.

Local Optimization with Higher Accuracy Methods

Outside of the domain of simple empirical potentials, identifying the global minima of cluster PESs becomes a prohibitively demanding task. Therefore, most studies on the theoretical determination of cluster minima employ methods that either focus on local minima obtained through an adequate initial guess or a mixture of global search algorithms with simple potentials to reduce the number of minima followed by local minimization techniques that are more accurate.

The majority of elements, regardless of whether they prefer atomic shells or electronic shells form clusters that are more or less spherical. The only elements that deviate from this behavior is the group IVA elements. This is especially remarkable in carbon, which goes from linear chains all the way to fullerenes. Clusters of Si and Ge first grow in one dimension and then abruptly change to form spherical clusters (Shvartsburg and Jarrold 1999). Some similarities exist between the growth patterns of Si and Ge cluster but major differences also occur especially concerning the size at which transition to bulk-like structures takes place (Shvartsburg and Jarrold 1999).

Because Si clusters undergo such a drastic change in cross section, an excellent experimental technique exists for studying the structure as a function of size. This technique (Jarrold and Constant 1991) is based upon the difference in the mobility of cluster ions that have different shapes. The ion mobility of a cluster depends on its rotationally averaged collision cross section, which depends on its size. Prolate and oblate geometries have a larger cross section and therefore smaller mobilities (Sieck et al. 2003). Mobility studies indicate that Si_n clusters undergo a phase transition at about $n = 24\text{--}34$ from elongated to spherical whereas for the Ge clusters this transition size is between $n = 64$ and $n = 74$ (Jarrold and Constant 1991; Shvartsburg and Jarrold 1999).

The growth sequence of Si is realized by adding on small building blocks to smaller structures. In particular, Si_9 (Shvartsburg and Jarrold 1999) and Si_{10} (Baletto and Ferrando 2005) have enhanced stability and, therefore, act as the fundamental building blocks. On the other hand, medium-sized Si clusters are quasispherical but not crystalline. Crystallinity does not become apparent until N gets as large as a few hundred atoms (Baletto and Ferrando 2005).

In the simulated annealing and DFT-based tight-binding work by Sieck and coworkers (2003), a *prolateness parameter* is defined as follows

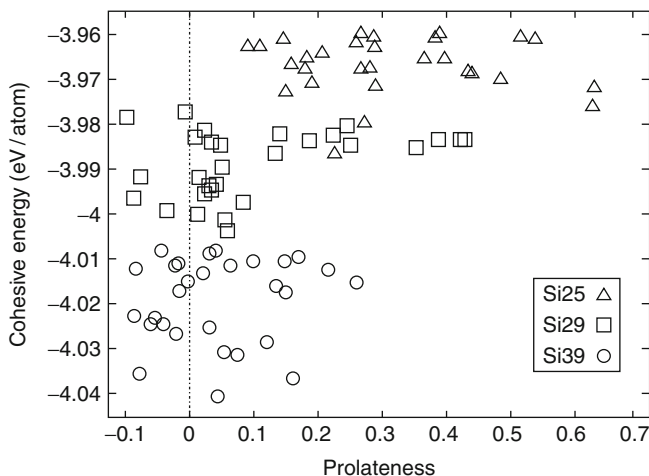
$$p = \sum_{j=1}^3 (I_j - \hat{I}) = -\frac{I_1}{2} + I_2 - \frac{I_3}{2}, \quad (27.3)$$

where $0 < I_1 \leq I_3$ and $\hat{I} = (I_1 + I_3)/2$. For an oblate structure $p < 0$, for a prolate structure $p > 0$, and for a spherical structure $p = 0$. Sieck and coworkers (2003) studied various different isomers corresponding to three fixed sizes, namely, $N = 25, 29$, and 35 . In  Fig. 27-3, the cohesive energy versus the prolateness parameter for the low-lying isomers is displayed. An investigation into the most stable structures clearly indicate the tendency to go from elongated to spherical structures as the clusters grow in size.

An important point is noted by Sieck and coworkers (2003), which is that different methods, even different flavors of the same method (LDA/GGA in DFT) may disagree about the exact energetic ordering of clusters, however, usually the lowest energy structures are local minima in all of them.

As an example to the multiscale methods mentioned above Bulusu and coworkers (2005) used a basin-hopping algorithm combined with DFT to explore low-lying minima for $\text{Ge}_{12\text{--}20}$. Global minima for the Ge clusters in this size range is compared to minima of Si clusters. Various checks were performed to make sure different starting points yield the same global minima, such as different seeding patterns. Unlike most studies in the literature, zero-point motion is taken into account while calculating the binding energies.

In the same work (Bulusu et al. 2005) of Si and Ge clusters in the size range 12–20 were compared and clusters of both Si and Ge were shown to have prolate geometries. However, their growth patterns were found to diverge at $N = 13$. The global minima for Ge clusters of



■ Fig. 27-3

Cohesive energy versus prolateness parameter defined in Eq. 27.3 for 30 lowest lying isomers of Si_{25} , Si_{29} , and Si_{35a} (Reprinted with permission from Sieck et al. (2003). © (2003) by Wiley-VCH)

size 12–16 are obtained by adding atoms to the Ge_9 tetracapped trigonal prism (TTP) structure familiar from Si clusters (Bulusu et al. 2005). For low energy Si clusters TTP-to-six-fold puckered ring(six/six) transition occurs at $N = 16$ and clusters with higher number of atoms all contain the six/six pattern. In contrast, TTP-to-six/six pattern may occur at $N = 19$ for Ge clusters and at $N = 20$, the magic number cluster Ge_{10} appears to be the preferred structural motif.

According to Shvartsburg and Jarrold (1999), clusters of Sn up to $n \approx 35$ follow the trend of germanium and prolate silicon clusters (Shvartsburg and Jarrold 1999). For $N > 20$, the mobility of Sn clusters show larger fluctuations than either Si or Ge. This might indicate the presence of multiple isomers of Sn clusters in this size range (Shvartsburg and Jarrold 1999). Even though the $\alpha \Rightarrow \beta$ transition occurs between 286 K and ≈ 310 K in the bulk, Sn clusters do not undergo such a transition even at higher temperatures. In fact, mobility measurements show that Sn clusters do not show significant changes in structure for a very broad temperature range. Transition from prolate to spherical growth in Sn clusters is not abrupt like the transition in Si and Ge clusters but occurs in steps. Clusters of $N \leq 35$ adopt a stacked prolate morphology much like Si and Ge clusters. This is unexpected because these highly noncompact structures are suitable for covalent materials whereas bulk Sn under ambient conditions is a metal. In a sense, the covalent-to-metal transition that occurs between the fourth and fifth row of the periodic table for the carbon series in the bulk fail to occur in their clusters. Shvartsburg and Jarrold (2000) also find that Pb_n^- and Pb_n^+ clusters display different magic numbers.

Going down the group IV in the periodic table a comprehensive set of data is given by Shvartsburg and Jarrold (2000). Their findings reveal that Pb clusters are structurally different from Si, Ge, and Sn cluster for $N < 25$. While the latter clusters have low mobilities in this size range indicating a prolate structure, Pb clusters exhibit much higher mobilities meaning they are quasispherical in shape. For $N > 25$, Si clusters also display mobilities in accord with a spherical shape. However, their mobilities are considerably smaller than the Pb clusters in the

same size range. This is attributed to the densely-packed nature of the Pb clusters in contrast with the open, cage-like arrangement of the Si clusters.

Transition metals form the largest group of elements considered in this section. Even as bulk materials, they exhibit very interesting and diverse properties, in particular magnetism. Interesting questions therefore arise concerning whether such properties as magnetism are maintained or altered in clusters (Briere et al. 2002; Kabir et al. 2006). Appearance of magnetism in the clusters of $4d$ elements (such as Ru, Rh, and Pd) is a very interesting phenomenon as these elements are nonmagnetic in the bulk. Clusters of $3d$ elements (such as Fe, Co, and Ni), which are already magnetic in the bulk, exhibit enhanced magnetic moments in the cluster form due to narrower band widths and the increased localization of the electrons (Kumar and Kawazoe 2002; Pawluk et al. 2005). Indeed, a recent Stern–Gerlach experiment revealed that Mn clusters in the range $N = 11$ –99 display ferromagnetic ordering even though no such ordering is observed in the bulk phase (Knickelbein 2001). These results reveal PES minima at $N = 13$ and $N = 19$ and PES maxima at $N = 15$ and $N = 23$ –25.

We should mention here that most of the magnetism studies mentioned in this section take into account only the electronic spin contribution to the magnetic moment. This can be done only in the cases where the spin-orbit coupling can be neglected.

In the work by Rodríguez-López and coworkers (2003), Co clusters in the range $N = 4$ –60 were studied by means of an evolutive algorithm based on the Gupta potential and tight-binding. Experiments reveal that much like the Cr clusters (Payne et al. 2006), different isomers of Co clusters coexist with distinct magnetic moments. In this work two sets of isomers are identified for each size – the lowest and the second-lowest lying. For the lowest-lying isomers an icosahedral growth is observed with structures derived by adding atoms to the main icosahedral sizes at $N = 7, 13, 19, 23, 26, 34, 43,$ and 55 . For the second isomers no particular growth pattern was identified. The stability of these sizes were also confirmed by the second energy difference ΔE_2 in addition to other, intermediate icosahedral structures.

Relative thermodynamic populations of the lowest-energy isomers were used to simulate possible experimental conditions. Isomers coexist particularly evenly between sizes of enhanced stability. This is due to the influence of the entropic contribution of the low-frequency normal modes of the isomers to the free energy. For both the global minimum and the second isomer, a nonmonotonic decrease is observed with increasing size. The greatest difference between the two sets of clusters arises in the range $N = 20$ –40, which corresponds to the range where the average interatomic distance and average coordination of the two sets show significant difference. In this size range, two effects seem to compete for determining the magnetization of the two sets of configurations. On the one hand, the average coordination is higher for the global minima, which should result in lower magnetic moments for the global minima. On the other hand, the average nearest-neighbor distance is higher for the global minima, which should yield higher magnetic moments. The results indicate that the average coordination number effect dominates.

For noble and transition metals, the interactions between atoms are not pairwise and simple empirical potentials are inappropriate (Barreateau et al. 2000). Therefore incorporating many-body effects into the potentials is essential. Moreover, for magnetism studies, *ab initio* methods need to be employed, which render global optimization efforts extremely computation-intensive. Therefore, most results we shall quote here will be based on restricted searches of the potential energy surface.

In the work by Barreateau and coworkers (2000), for instance, the relative stability of cuboctahedra and Mackay icosahedra is determined for Rh and Pd clusters for $N = 13, 55, 147, 309,$ and

561 using a tight-binding method. Since both structures have an identical sequence of magic numbers it is interesting to determine the transition size. A continuous transition is possible from the Mackay icosahedron to the cuboctahedron, and for the Rh and Pd clusters, this pathway is explored. An analysis of the Mackay transition from the cuboctahedron to the icosahedron reveals that for $N = 13$, the cuboctahedron is unstable for both Rh and Pd, becoming metastable for larger sizes with an increasing activation barrier with size. The magnetic moment of rhodium was found to disappear for sizes more than 100 atoms, and palladium clusters were found to be hardly magnetic.

In Mn clusters, on the other hand, magnetism plays an important role in determining the ground state structures. As mentioned in the work by Briere and coworkers (2002), many spin isomers can lie close in energy. In this work, a few local geometric configurations of $N = 13$, 15, 19, and 23 were studied using spin-polarized calculations. At all sizes except $N = 15$, the structure with the lowest energy was found to be icosahedral. For $N = 15$, a bcc configuration was found to be favorable. In terms of spin, all the structures were found to be ferrimagnetic with alternating domains of different spin configurations (see  Fig. 27-4). Except for $N = 15$, the mean value of the integrated spin density was found to decrease with increasing size.

In the DFT work by Kabir and Mookerjee (2006), the ground state structure for Mn_{13} was found to be the icosahedron with the two pentagonal rings that are coupled antiferromagnetically. Therefore, the resulting magnetization is small, namely, $0.23\mu_B/\text{atom}$. This magnetization is considerably smaller than the neighboring sizes 12 and 14. The $N = 14$ structure differs from the $N = 13$ structure by a single capping atom. However, the presence of this atom changes the magnetization arrangement considerably. In this case the pentagonal rings are ferromagnetically coupled and the magnetization is $1.29\mu_B/\text{atom}$. The case of Mn_{15} is worth mentioning because of the discrepancy between two DFT studies by Briere and coworkers (2002) and Kabir and Mookerjee (2006). In the latter, the ground state structure was found to be icosahedral with a magnetic moment of $0.87\mu_B/\text{atom}$ whereas Briere et al. (2002) found a bcc

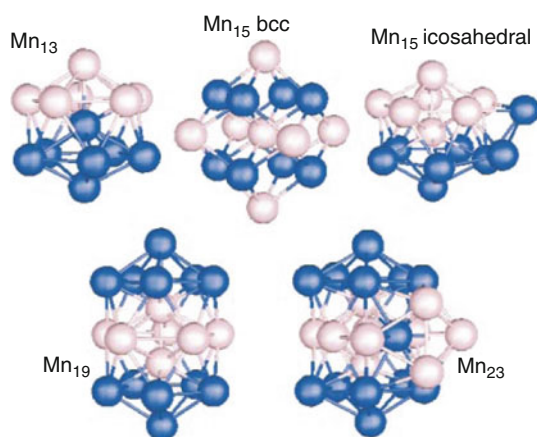


 Fig. 27-4

Lowest energy structures of some Mn clusters. Relative spin alignments are marked with dark for spin up and light for spin down (Reprinted with permission from Briere et al. (2002). © (2002) by the American Physical Society)

structure with $0.20\mu_B/\text{atom}$. For $N = 19$, a double icosahedron was observed, which again has a smaller magnetic moment, $1.10\mu_B/\text{atom}$, than its neighboring clusters. The central pentagonal ring is AFM coupled to the neighboring pentagonal rings. This behavior is persistent in the $N = 20$ cluster, which has a magnetic moment of $1.50\mu_B/\text{atom}$. In the range $N = 11 - 20$, spin segregation is observed, where like spins tend to cluster. The binding energy is observed to increase monotonically with increasing size. This is due to the increased sp bonding. However, when compared with other transition metals, Mn clusters remain weakly bound.

An interesting property of Ta clusters were demonstrated in a recent study (Fa et al. 2006), where ferroelectricity and ferromagnetism was proven to coexist. Initial structures were obtained by simulated annealing using an empirical potential. These structures were later reoptimized with DFT calculations. The magic numbers for Ta clusters were found to be 4, 7, 10, 15, and 22. It was therefore deduced that Ta clusters do not prefer icosahedral growth. For $N = 13$, for instance, the lowest energy structure among those studied was found to be a distorted five-capped hexagonal bipyramid. For $N = 19$, the most stable structure is decahedral in contrast with the double icosahedron, which was found to be stable for many other clusters. No perfectly symmetric structures were found indicating that Jahn-Teller distortions play an important role in determining the ground state structures of Ta clusters. In the size range studied in this work (Fa et al. 2006), the atomic packing shows differences such that each size behaves like an individual system rather than steps of a continuous growth sequence. In addition, electronic dipole moment and magnetic moment were also calculated. The electronic dipole moment was found to have the same trend as the *inverse coordination number*, which is a parameter that reflects the asymmetry of the cluster. This agreement is attributed to the strong correlation between the structure and the electronic dipole moment of the clusters. Odd- N Ta clusters also display a magnetic moment of about $1\mu_B$, which suggests the possibility of the coexistence of ferroelectricity and ferromagnetism. The growth pattern of Ta was found to be very similar to that of Nb. However, when compared with vanadium clusters, this similarity is absent (Fa et al. 2006).

In a similar work by Fa and coworkers (2005), Nb clusters were also found to display ferroelectricity supported by a recent experimental study. This is an important discovery because ferroelectricity was never observed in single element bulk materials. For $N \geq 38$, the electric dipole moment exhibits even-odd oscillations. This suggests that there is a strong correlation between the structure and the ferroelectricity.

In the work by Pawluk and coworkers (2005), the structure and stability of several Ir clusters were studied using DFT. Rather than using a global optimization algorithm, possible configurations both truncated from bulk and built independently were relaxed locally. The results indicate that Ir clusters mostly prefer cube-like structures up to $N = 13$, except for $N = 11$, which assumes an elongated structure. At $N = 13$, the lowest structure among the ones studied is the icosahedron. This is in contrast with Ru and Pt, which prefer simple cubic structures. When compared to clusters cut from the fcc bulk, simple cubic structures turn out to be more stable up to a size of $N = 48$. This transition occurs near $N = 40$ in Ru and $N = 13$ for Pt. Another interesting property studied in this work is the fluidity of clusters. The results indicate that while the Pt clusters exhibit a more fluidlike character and will thus easily coalesce with other clusters, Ir clusters are more rigid and have less tendency toward coalescence.

An interesting experimental result concerning Pt clusters was reported by Liu and coworkers (2006), who found that Pt_{13} clusters exhibit substantial magnetism (about $0.65\mu_B/\text{atom}$) even though bulk Pt is not magnetic.

Although for such clusters as Ni and Au the icosahedral structure is calculated to be metastable with stability decreasing with size, experiment reveals that icosahedral structures are found in clusters containing several thousands of atoms. This means that kinetic effects are also very important in determining the structure of a cluster (Gafner et al. 2004). In order to simulate these kinetic effects, a 555 Ni cluster was studied using tight-binding by Gafner and coworkers in (2004). The cluster was heated to 1,800 K ($T_{melt} = 1,145$ K) and subsequently cooled to 300 K. The melting and crystallization curves are determined from a sudden change in the potential energy as a function of temperature. They found that slow cooling results in an fcc structure whereas fast cooling results in the formation of a metastable icosahedral structure.

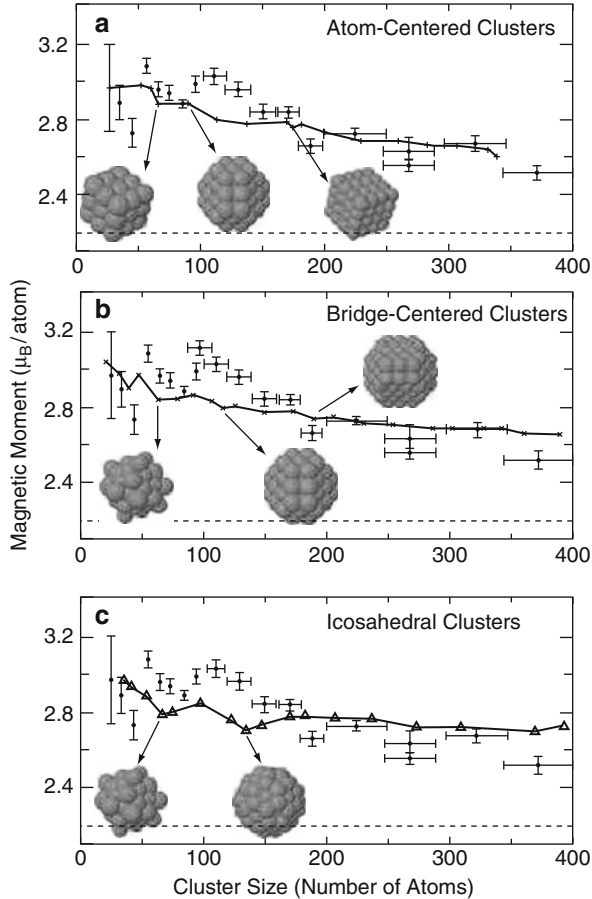
In the study by Köhler and coworkers (2006), the potential surface of a few sizes ($N = 13, 53-57$) of Fe clusters were mapped out with respect to magnetization and volume change using a DFT-based tight-binding scheme. Icosahedra were found to be the most stable structures for the magic numbers $N = 13$ and $N = 55$. Two local minima were observed for the $N = 13$ icosahedron, one ferromagnetic and one antiferromagnetic. The PESs for clusters with $N = 53-57$ were mapped out using a genetic algorithm-based procedure. Derivatives of the $N = 55$ structure were considered for $N = 53, 54, 56$, and 57 . Generally icosahedra and icosahedron-derived structures have relatively small magnetic moments. The structures without apparent symmetry show higher magnetic moment than icosahedra. No ferromagnetic ordering was found for the Fe_{55} cluster.

Tiago and coworkers provide a very comprehensive explanation of the origin of magnetism in small Fe clusters in their article (Tiago et al. 2006). In the Fe atom, the magnetic moment is a result of exchange splitting. The $3d_{\uparrow}$ states are occupied by 5 electrons, while the $3d_{\downarrow}$ states are occupied by a single electron, which results in a rather high magnetic moment of $4\mu_B$. When the atoms come together to form a crystal, hybridization of the large 4s bands and the 3d bands reduce the magnetism down to $2.2\mu_B$. In clusters, hybridization is not so strong because of the reduced coordination numbers of the surface atoms. Because this hybridization depends on orientation, clusters with faceted surfaces are expected to have different magnetic properties than those with irregular faces. According to Tiago and coworkers (2006), this effect is the likely cause of the nonmonotonic suppression of magnetic moment as a function of size. Two classes of Fe clusters were considered in this work: faceted and nonfaceted. Nonfaceted structures are nearly spherical in shape and faceted structures are built using the conventional layer-by-layer growth model. The magnetic moment was calculated as the expectation value of the total angular momentum,

$$M = \frac{\mu_B}{\hbar} [g_s \langle S_z \rangle + \langle L_z \rangle], \quad (27.4)$$

where $g_s = 2$ is the gyromagnetic ratio of the electron. The magnetic moments of the clusters as a function of size is displayed in  Fig. 27-5 for all classes of clusters considered. Suppression of the magnetic moment with increasing size is observed, in good agreement with experiment. Clusters with faceted surfaces indeed have a lower magnetic moment due to more efficient hybridization although the correlation of shape and magnetic moment is not always well defined. Icosahedral structures are predicted to have magnetic moments lower than bcc clusters.

Another good example of disagreement between different methods is given in Krüger and coworkers where Pd clusters having several high-symmetry structures including icosahedra, octahedra, and cuboctahedra were optimized using both the LDA and GGA in the DFT framework. GGA yields larger bond lengths in accord with the general expectation. But the difference is almost independent of size. Icosahedral structures tend to yield larger bond lengths



■ Fig. 27-5

Magnetic moments of faceted and nonfaceted Fe clusters in the icosahedral and bcc configurations: (a) atom-centered bcc, (b) bridge-centered bcc, and (c) icosahedral. Experimental data is displayed as black diamonds for comparison (Reprinted with permission from Tiago et al. (2006).

© (2002) by the American Physical Society)

than octahedral and cuboctahedral structures, also displaying a flatter variation with increasing coordination number. The accuracy of this *breathing mode* relaxation was confirmed by comparing to a full relaxation of the Pd₅₅ cluster.

The Pd₁₃ cluster was found in the work of Kumar and Kawazoe (2002) to have an icosahedral structure with a $0.62\mu_B/\text{atom}$ magnetic moment. This result agrees with some of the earlier studies and disagrees with some others. The central atom in the cluster is found to have a smaller magnetic moment than the surface atom only by a very small amount unlike the large difference in the Mn₁₃ study of Kabir and coworkers (2006). For $N = 14$ and 15 icosahedron-derived structures are favored over other high-symmetry structures. The magnetic moments for both sizes remain around $0.5\mu_B/\text{atom}$. Going from $N = 16$ to the double icosahedron at $N = 19$, the magnetic moment decreases from $0.38\mu_B/\text{atom}$ to $0.32\mu_B/\text{atom}$. As the cluster sizes increase

there is a decrease in local (atomic) magnetic moments. For $N = 55$ and $N = 147$, the lowest-lying state was found to be the Mackay icosahedra. Cubic and decahedral structures were found to have the next highest energies, with $0.29\mu_B/\text{atom}$ and $0.41\mu_B/\text{atom}$ respectively. For the Pd_{55} cluster, structures with smaller magnetization lie very close to the ground state and would therefore be accessible at room temperature. So magnetic order can be easily lost under experimental conditions. In contrast to the results for Mn (Kabir et al. 2006), the icosahedral structures have a higher magnetic moment than other high-symmetry structures.

In work of Nava and coworkers (2003), Pd clusters were studied using the spin-polarized DFT method in the range $N = 2$ –309. The $N = 13$ cluster was found to have an icosahedral structure with a high spin state. It is seen to undergo a very slight Jahn-Teller distortion, which increases the cohesive energy only by 0.01 eV. The truncated decahedron and the cuboctahedron are found to be less stable.

Yao and coworkers (2007) utilized results from simulated annealing of Ni clusters using an empirical potential as starting configurations to further optimize them using a DFT code. This is another technique often used in cluster literature. In this work, Ni clusters with $N = 10$ –27 atoms were found to attain icosahedron-like structures with the $N = 13$ cluster being a perfect icosahedron and $N = 19$ the double icosahedron. Clusters in the range $N = 28$ –40 have very complicated structures because they are in the transition region between the $N = 13$ icosahedron and the $N = 55$ icosahedron. Around $N = 19$ and $N = 55$, clusters are mostly formed by adding or removing a few atoms from the corresponding perfect icosahedra. Dips are observed in the magnetic moment for $N = 13$ and 55 as expected from the compact structure of these clusters.

While all of the studies mentioned above deal with collinear spin, which singles out one direction along which the magnetic moment may be oriented, a very important class of clusters with high magnetic moments display noncollinear spin. In these clusters, the magnetic moment is allowed point in an arbitrary direction and thus present a new degree of freedom. A good example for the investigation of this effect is presented in the work by Du et al. (2010) where 6-atom clusters of Co and Mn atoms with several different compositions but always in the octahedral geometry were investigated within the DFT theory including the noncollinear spin formalism. Low-lying isomers with up to more than 40° of average degree of noncollinearity were identified. For certain compositions and geometries different tendencies for magnetic coupling (AFM vs FM) is also found to cause a certain degree of spin frustration.

In the work by Zhang and coworkers (2004), Mo clusters were studied within the DFT framework. An interesting result was that the initial icosahedral structure for the $N = 13$ cluster was found to undergo a very large distortion. This distortion was explained by the tendency of Mo clusters to form Mo dimers. The strength of the bonds in Mo_{13} is covalent, therefore, at this size, the cluster shows nonmetallicity. At $N = 55$, the icosahedral structure is found to again undergo a large distortion. However in contrast to $N = 13$, the alternate O_h structure was not found to be much more stable than the distorted icosahedron. This was explained by the decrease of nonmetallicity with size.

1D Structures: Nanotubes, Nanowires, Nanorods

In nanoscience literature, the name *one-dimensional* was coined to describe systems where one of the dimensions is several orders of magnitude larger than the other two dimensions. Much like the zero-dimensional case, the border between one- and two-dimensional systems is

ill-defined and system-dependent. For this reason, two-dimensional systems exhibit the same richness in structural and electronic properties as in the zero-dimensional case unlike their bulk counterparts.

One, dimensional structures may, in the broadest classification, be divided into nanotubes, nanowires, and nanoribbons. *Nanotubes* are simply described as two-dimensional materials (such as graphene, BN sheets, TiO₂ sheets and many others) seamlessly rolled into a hollow cylinder although the actual fabrication usually follows a much more involved procedure. Nanotubes may be regarded as a unique subset of one-dimensional structures that do not have a surface and are thus devoid of surface effects. In this respect they are analogous to the fullerenes in the zero-dimensional case. *Nanowires* on the other hand are extremely thin wires that are grown or extracted along well-defined crystal directions and may have widely different surfaces. The surfaces, however, rarely remain in their bulk configuration and often reconstruct to reduce strain or saturate broken bonds. This procedure is highly size- and material-specific, and nanowires therefore display a large variety of strongly surface-dependent properties. Finally, *nanoribbons* are thin strips of two-dimensional materials such as graphene. The edges may reconstruct or be saturated with different species to modify their properties.

In addition to structural and electronic properties that are explored in zero-dimensional materials, one-dimensional materials also exhibit rather interesting elastic properties. We shall begin this section with a brief review of elastic considerations regarding one-dimensional nanomaterials and afterward move onto structural and electronic properties.

Elastic and Structural Properties

In nanowire applications such as AFM tips, NEMS, and MEMS, which make use of mechanical properties, it is crucial to have a good understanding of the evolution of elastic properties all the way down to the nanoscale. Elastic properties that are ordinarily under investigation include elastic moduli, plasticity, crack propagation, buckling, and breaking points.

There are numerous examples of experimental determination of elastic properties of nanowires in the literature. A recent study by Barth and coworkers (2009) determines the Young's modulus of SnO₂ nanowires by anchoring and bending them with the help of an AFM tip. By mapping the bending amplitude to the Young's modulus through classical elasticity formulae the Young's modulus is estimated at around 110 GPa for the samples studied.

Contrary to the macroscopic scale, the elastic properties of nanoscale one-dimensional systems are often seen to depend on their physical dimensions. This intriguing fact brings forth the necessity of studying, among others, the elastic properties of such systems as a function of their size. In fact, the theoretical literature is very rich in examples of such studies. Empirical potentials are particularly suitable for studies of size dependence since systems with large numbers of atoms may be handled with relative ease, allowing the determination of convergence of elastic properties of nanomaterials to those of their bulk counterparts. A related question to this fact is to what extent the laws of continuum elasticity can be applied to nanoscale systems, which has received much attention both theoretically and experimentally. A recent study by Rudd and coworkers (2008) opens with this very same question, where the Young's modulus of Ta {001} and Si{001} nanowires has been determined using a Finnis-Sinclair (1984) and Stillinger-Weber (1985) potential respectively in a molecular dynamics simulation. Nanowire radii were explored up to approximately 10 nm and both materials were found to display a

strong dependence on the wire width eventually converging to the bulk value. Interestingly, the convergence trends are opposite where the Young's modulus of the Si nanowires increases while that of Ta nanowires decreases with radius. In the same study, DFT calculations were also performed on Si nanowires, partially confirming the outcome of the Stillinger-Weber calculations. However, the match with continuum theory was found to be much better for the DFT results.

Size-dependence is also demonstrated in a study by Hu and coworkers (2008) on ZnO nanowires and nanotubes where they use an exp-6 type empirical potential including Coulomb interaction for Young's modulus calculations. The Young's moduli of nanowires and nanotubes show a very strong dependence on the radius and wall thickness respectively.

Due to the extremely high surface-to-volume ratio in nanowires, the particular surfaces that are exposed at the outer edges of the nanowires play a crucial effect in the determination of their elastic properties. Recent evidence for this fact was demonstrated by Wang and Li (2008) in their DFT-parameterized model study of Ag, Au, and ZnO nanowires with different surface terminations. Their results show discernible albeit small differences in the size dependence of the Young's modulus for different surface terminations of the nanowires in question.

Nanotubes have also received a great deal of attention from researchers due to their extraordinary elastic properties. They have been shown to possess an unusually high axial stiffness in addition to very high reversibility under large distortions. In addition to the large body of literature on experiments probing the elastic properties of nanotubes, many theoretical studies have also been conducted. Due to their varying radii and chirality, nanotubes present endless possibilities for the investigation of their elastic properties. Liang and Upmanyu (2006), for instance, have studied the radius (or equivalently curvature) and chirality dependence of the torsion induced by applied axial strength of the nanotubes. Their studies, which utilize the widely used second-generation reactive empirical bond-order potential (Brenner 1989), revealed a torsional response of up to 0.75° nm, which varied remarkably for different radii and chiral angles. Conversely, as reported in several early studies on nanotubes employing DFT calculations, Young's modulus is known to be largely independent of the chirality.

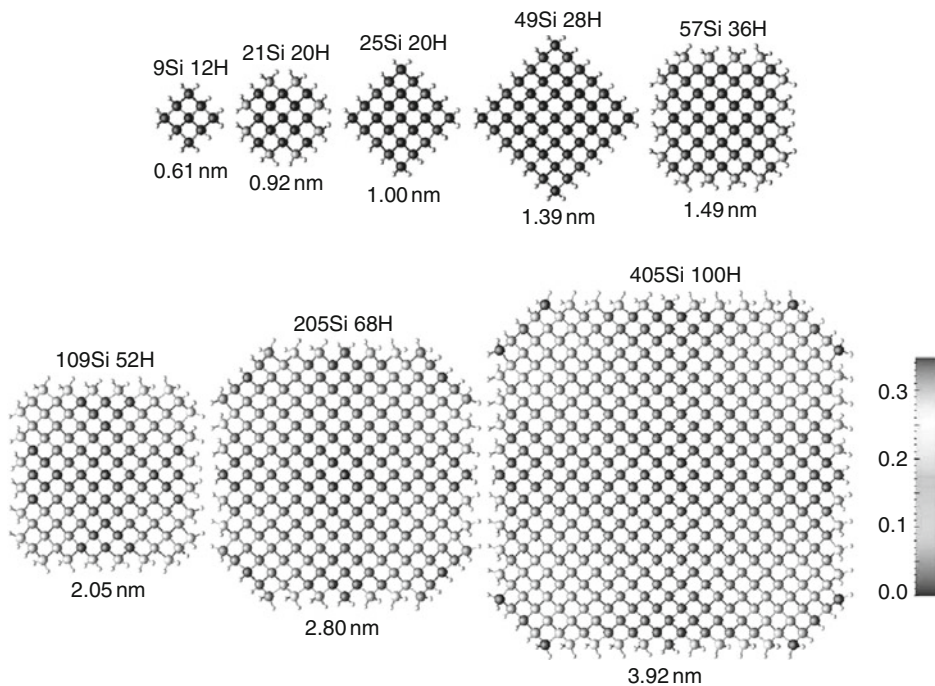
Elastic properties of nanotubes of many materials other than C have also been theoretically explored. In an exhaustive work, Baumeier and coworkers (2007) used DFT calculations to survey such properties as strain energy and Young's modulus of SiC, BN, and BeO nanotubes. Baumeier and coworkers observe that being composed of two atomic species instead of one as in carbon nanotubes, the nanotubes made out of these materials exhibit a different relaxation pattern for the relevant anions and cations, suggesting possible different behavior than carbon nanotubes. Nevertheless, the results show that at least for (n, n) and $(n, 0)$ nanotubes of similar radii the behavior is similar. All three materials display a decreasing Young's modulus as a function of radius converging to the sheet value for large radii. Among the three materials, BN nanotubes display a significantly high Young's modulus, followed by SiC and finally by BeO nanotubes.

The interwall attraction in multi-walled nanotubes opens up another possible avenue for the study of elastic properties. Zhang (2008) and coworkers have studied the Young's modulus, Poisson ratio and the buckling point of multi-walled nanotubes using a combination of second-generation reactive bond-order potential to model intralayer bonding and a Lennard-Jones potential for the interlayer interaction. The multi-walled nanotubes studied were divided into two sets, the first formed by embedding increasingly smaller (n, n) tubes into a large $(20, 20)$ nanotube (up to four walls) and the second by placing a $(5, 5)$ tube into increasingly larger (n, n) tubes (again up to four walls). A molecular dynamics algorithm was used during their

calculation and the dependence of the moduli in addition to the buckled morphologies were presented. Young's modulus and Poisson's ratio turn out to follow a different trend for the two sets considered. While the set that grows inward display increasing (decreasing) Young's modulus (Poisson ratio) for increasing number of walls, the set that grows outward follow the opposite trend.

As mentioned in the introduction to this section, one way to saturate the surface bonds of nanowires is through passivation by different species. The elastic behavior of passivated versus unpassivated nanowires raises an interesting question. Lee and his coworkers (2007) studied several elastic properties of H-passivated nanowires of a large range of radii varying between 0.61 nm and 3.92 nm (see ► Fig. 27-6) using DFT. As expected, the Young moduli of H-passivated Si nanowires mostly follow predictions from continuum models regardless of the varying proportions of $\langle 100 \rangle$ and $\langle 110 \rangle$ surfaces exposed. This is attributed to the fact that the bulk-like covalent bonding character at the surfaces is preserved when H is used to passivate the dangling bonds at the surface.

Although microscopic modeling is of utmost importance in the understanding of nanoscale materials, there are a number of experimental situations of interest that cannot be handled by these time-intensive methods due to their large size. For large enough systems (such as large portions of nanotubes suspended over a trench) continuum methods may be employed (Ustunel et al. 2005). However, complete coarse-graining is also not always a viable choice since one then loses detailed information on locally nonhomogeneous regions of the system such as defects



■ Fig. 27-6

H-passivated Si nanowires of different sizes studied by Lee et al (Reprinted with permission from Lee and Rudd (2007). © (2007) by the American Physical Society)

and local deformations. In such cases, *multiscale methods* which apply different methods at different scales of the system are the methods of choice. An illustrative example was studied by Maiti (2008) where a micromechanical sensor made out of a nanotube was deformed by a Li needle. The bent but undeformed portions of the nanotube were modeled by a coarse-grained *molecular mechanics* simulation, while the highly deformed midsection (enclosed in a box) was modeled using a quantum mechanical method. The two methods were then matched at the interface of the two regions.

Structural Properties

The novel electronic properties of nanotubes, nanowires, and nanobelts are inextricably linked to their structural properties. This is largely due to their high surface-to-volume ratio, where the bonding on the surface structure determines the electronic states which in turn determines such properties of the system as conductivity and magnetism.

As mentioned in the introductory section, nanowires nowadays may be manufactured from a great variety of materials. As fabricated, it is experimentally difficult, if not impossible, to intuitively infer their surface structure. Simulations on the other hand provide an inexpensive yet accurate way of studying this relation between structure and electronic properties.

The methods of preference in nanowire modeling is generally tight-binding and to a larger extent DFT, since electronic properties depend sensitively on the structure requiring accurate calculations. Once a material (or combination of materials) is chosen the important parameters of nanowire modeling are the particular surfaces surrounding the nanowire and passivation, that is, the saturation of the bonds at the surfaces. Two of the most commonly studied surface terminations are surface reconstruction and H-passivation.

Due to the axial periodicity of one-dimensional nanomaterials, plane wave-based methods which are traditionally used for crystals are very often employed. In the work of Arantes and Fazio (2007), where they study free and passivated Ge nanowires, the band gap of passivated and unpassivated nanowires were determined using a plane wave-based GGA-DFT method. The nanowires were grown in the $\langle 110 \rangle$ and $\langle 111 \rangle$ directions and their band gaps were calculated as a function of nanowire diameter. In spite of the well-known underestimation of the band gap by LDA and GGA methods, a trend can be obtained rather reliably. The band gaps are seen to vary with respect to direction and size.

Though not often encountered global search algorithms are also used for determining the structure of nanowires. Especially in the case of nanowires with smaller radii, the structure may be so different from bulk as to prevent any *a priori* prediction. Chan and coworkers (2006) conducted a genetic algorithm search based on the formation energy of H-terminated Si NWs where the formation energy is defined as

$$f = (E - \mu_H n_H) / n - \mu, \quad (27.5)$$

where E is the total energy of the NW in question, μ_H and μ are the chemical potentials of H and Si respectively, and n is the number of Si atoms. The genetic algorithm was conducted in two stages. In the first stage a long evolution through several generations was conducted using an empirical potential (of the Hansel-Vogel type). In the second stage the outcome structures of the evolution for each size were relaxed using a DFT algorithm. The result, reminiscent of cluster structures, is that certain sizes of Si NWs are preferred over other sizes. These structures are once again termed *magic sizes*. In general, structures with even number of Si atoms are preferred over

those with an odd number. The most stable structures are observed either in a *plate-like* form where chains of Si hexagons join together to form flat structures, or a *hexagon-shaped* cross section.

One of the most important parameters in determining the geometric and therefore the electronic structure of nanowires is surface termination. The high-energy dangling bonds at the surface may either be saturated by a rearrangement and rebonding of the surface atoms or by attaching electropositive species (such as H). In general, while the reconstruction may significantly alter the structural and electronic properties of the material, passivation by other species leaves these properties relatively unaltered. In the recent work of Migas and Borisenko (2008), $\langle 001 \rangle$ oriented Si nanowires were passivated by O, F and H and the structural and a large number of different sizes and geometries were studied using DFT. Under different combinations and coverages by these elements, the band gap of the Si nanowires considered (only nanowires with rhombic cross sections were considered) were found to vary between 1.20 and 1.96 eV, which shows that termination can be used as a means to control the electronic properties.

Countless other studies in understanding the structure of experimentally relevant one-dimensional structures have been done. Bi nanowires (Qi et al. 2008), CdSe nanorods with hexagonal and triangular cross sections (Sadowski and Ramprasad 2007), and Te nanowires (Ghosh et al. 2007) are some studies that may be mentioned. In addition to materials that have already been manufactured, researchers have also been interested in the possible existence and properties of nanoscale systems that have not yet been experimentally realized. Rathi and Ray (2008), for instance, have examined the possibility of SiGe nanotubes, while Qi (2008) and coworkers investigated Bi nanotubes and hollow Bi rods. Recently it was demonstrated by model calculations that the stable carbon nanotube structure might be possible with non-graphene like form (Erkoc 2004). Furthermore, nanorod structures constructed from benzene rings only (called as *benzorods*) may also be possible. Their structural and electronic properties were investigated by performing model calculations (Erkoc 2003; Malcioglu and Erkoc 2004).

Electronic, Magnetic and Optical Properties

As a result of the immense variation in structural properties of one-dimensional structures, one observes an equally diverse spectra of electronic properties. Perhaps the most intriguing property of one- and two-dimensional nanoscale systems is that after the required geometrical deformations in order to reach their equilibrium, one might observe a stark difference between the newly formed system and its bulk counterpart. A material which is an insulator in bulk may become a conductor when taken to the nanoscale. Similarly one- or two-dimensional nanostructures of a nonmagnetic material may have a nonzero magnetic moment. These differences usually stem from the new states introduced into the electronic structure of the material by terminating structures such as surfaces, steps, edges, and corners. The interest in these emergent properties is due to the possibilities of integrating these small-scale materials into technological applications and controlling their properties by controlling the structure.

Due to the ease of interfacing with current technology, Si nanowires have perhaps been the most intensely studied system. Rurali and Lorente (2005), for instance, explored a large range of surface reconstructions for $\langle 100 \rangle$ Si nanowires with a small radius of about 1.5 nm. They discovered that for certain reconstructions the nanowires develop conducting states in their band gap, while for others the semiconducting behavior is retained. This is a prime example of effects of confinement on the electronic structure of a system.

Another parameter that has a strong effect on the electronic properties of nanowires is surface termination. As demonstrated by Rurali (2005) that both Si and C-terminated H-passivated SiC nanowires have a larger band gap than that of bulk SiC. As discussed by Rurali, this is purely a confinement effect since passivation prevents reconstruction and the related introduction of gap states. However, when the nanowires are allowed to reconstruct, both species of SiC nanowires are seen to become conducting due to the surface states introduced into the band gap.

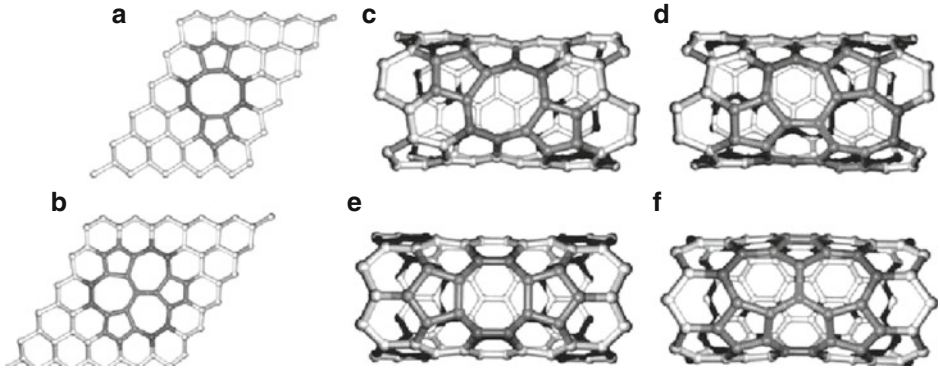
In addition to the conventional carbon nanotubes, several other materials were investigated as viable candidates for nanotube structures. BN (Chopra et al. 1995) and more recently (Sun et al. 2002) SiC nanotubes are two such materials which have been successfully synthesized in the nanotube form. Following their synthesis Gao and coworkers (2008) conducted a DFT-PAW study of undoped and N-doped SiC nanotubes of varying sizes. For each size the nanotubes were doped initially with 2 and 4 N atoms and their structural and electronic properties were studied. For each doping level, several possibilities were investigated and the most stable structure was identified. As an extreme case, the case in which all the C atoms were replaced with N atoms, in other words SiN nanotubes, was considered. These nanotubes, instead of being circular were found to have a staggered or star-like cross section. In all the cases considered the nanotubes were found to be semiconducting with an indirect band gap. Recent model calculations on binary compounds BN (Erkoc 2001), GaN (Erkoc et al. 2004), InP (Erkoc 2004), ZnO (Erkoc and Kokten 2005) nanotubes give reasonable results comparable with experimental findings.

Although by nature rather free of defects, the few existing defects in graphene and nanotubes change the electronic structure of their host material drastically (Pekoz and Erkoc 2008). In spite of the several experimental methods that have been developed to locate and study the properties of such defects, theoretical methods are an indispensable tool for creating isolated defects of the desired nature and studying their effects on electronic properties. A particularly interesting question is the stability of well-characterized graphene defects in nanotubes of varying radius and chirality. Since a graphene sheet can be viewed as a nanotube with an infinitely large radius, the formation energy of any nanotube defect should tend to the equivalent defect on a graphene sheet. Amorim et al. (2007) demonstrated an example of this behavior by studying the so-called 555777 defect, which is a combination of three pentagons and three heptagons. This defect is formed in two steps. In the first step two divacancies coalesce to form a new defect (585) composed of two pentagons and an octagon. This step is followed by a further structural change, which yields the 555777 defect, see  Fig. 27-7.

In graphene the 555777 defect is found to be more stable than the 585 defect by 0.8 eV. The same defects were then created in zigzag and armchair nanotubes of radius in the range of 7–15 Å. As in the graphene case the 555777 defect is found to be more stable in all the nanotubes studied. The formation energy is, however, lower than in the graphene case. The expected tendency toward the corresponding graphene values is seen in both cases and convergence is estimated to occur around a radius of 40 Å.

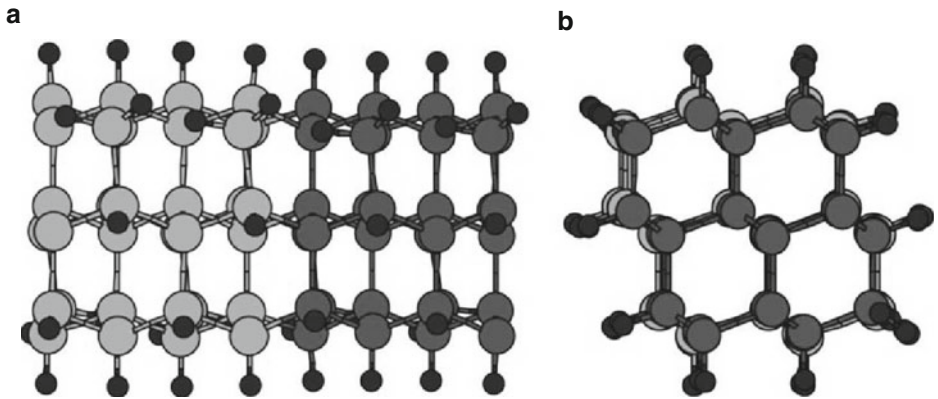
The effect of defects on the electronic properties of their host substance is illustrated in this work by the conductance graph calculated using the Green's function density functional theory. The results indicate that the presence of both the 585 and 555777 reduce the conductance considerably while at the same time displaying different voltage dependence.

Another investigation of defects in nanotubes for the purpose of application as a gas sensor was conducted by Andzelm and coworkers (2006). The particular question at hand is the binding of NH₃ molecule to nanotubes and whether or not binding is enhanced by defects. Three defects are considered: a Stone-Wales defect (a defect formed by rotating a given bond by 90°



■ Fig. 27-7

585 (a) and 555777 (b) defects in graphene and 585 (c,e) and 555777 (d,f) defects in a nanotube in different orientations (Reprinted with permission from Amorim et al. (2007). © (2007) by the American Chemical Society)



■ Fig. 27-8

A Si-Ge interface shaped into a nanotube. (a) Side view, (b) cross view (Adapted from Kagimura et al. 2007)

resulting in the formation of two pentagons and two heptagons), a monovacancy and an interstitial C atom placed on top of a bridge. In addition, the case of an O_2 molecule dissociated on a SW defect was also considered to mimic the environmental effects. Two different orientations, straight and chiral, for the SW defect were considered. All-electron DFT calculations reveal that the monovacancy is the most stable. Calculation of reaction barriers also reveal that defects with preabsorbed O dissociate NH_3 into NH_2 and H.

The heterostructure problem, which has been widely studied in the bulk form, is becoming an increasingly popular topic also in the one-dimensional systems. The band alignment problem has been addressed recently in a DFT study conducted by Kagimura and coworkers (2007) where a Si-Ge interface was studied. The model for such a system is shown in ► Fig. 27-8. The band states contributed by the surface dangling bonds were investigated as possible candidates for the induction of a potential well.

The search for nanoscale materials that exhibit spontaneous magnetization has become an increasingly rich field in the past decade. Several materials such as doped nanotubes and nanowires, defective graphene and nanoribbons of two-dimensional materials can be itemized as candidates considered in these studies. In order to identify the suitability of a material for spontaneous magnetization, electron density in the two spin channels, $n^\uparrow(\vec{r})$ and $n^\downarrow(\vec{r})$ are compared. If there is a significant difference in this distribution, the material is nominated for use in magnetic applications. If in addition the density of states in the two spin channels show different characteristics at the Fermi level such that in one channel there is a significantly larger number of states than the other, then the material provides promise also in *spintronics* applications.

One such candidate material for magnetic applications is BN sheets and nanotubes doped with several different elements. In a recent example, Li and coworkers (2008a), in their DFT study on BN nanotubes with one, two, and three H atoms adsorbed at different locations, observed that some of the configurations considered may give rise to a magnetic moment of up to 2.0. The origin of this magnetic moment is evident from the band structures where the contribution of band gap states are due to only one of the spin channels. The states that are seen in the gap are also shown visually and their origin is unambiguously identified as due to the adsorbed hydrogen.

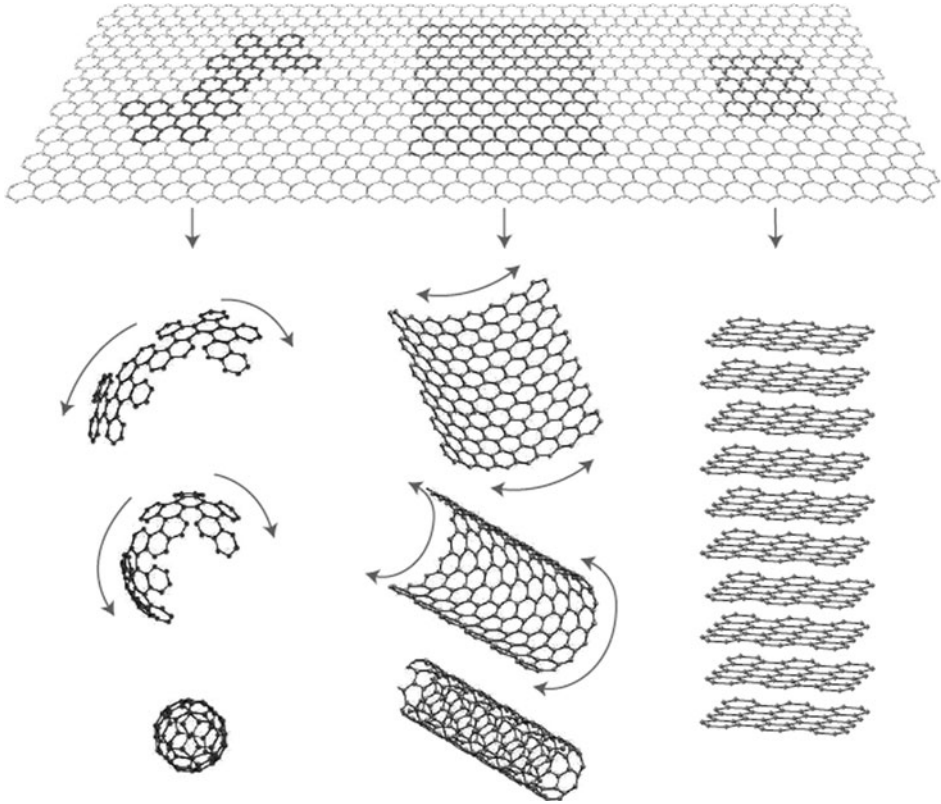
A rather novel and intriguing application of nanomaterials and its investigation using theoretical modeling is the subject of a recent work by Santos de Oliveira and Mina (2009). Their study discusses a phenomenon called *self-purification* of nanomaterials, namely, the expulsion of foreign species from the surface. Self-purification is attributed to the fact that nanoscale materials have a lower incorporation rate of impurities compared to their bulk counterpart. In this work SiC nanowires are studied as another potential example of self-purifying materials. B and N impurities were planted at different positions inside and on the surface of three SiC nanowire configurations ($\langle 100 \rangle$ Si-coated, $\langle 100 \rangle$ C coated and $\langle 111 \rangle$ Si and C coated) at locations ranging from the center to the surface. The formation energies of the configurations thus formed were then calculated and compared. As a result, the self-purification process was found to be favorable for B-doped SiC nanowires irrespective of their orientation. The B atom was found to segregate favorably to the surface and thus expelled. The N impurities, however, were found to prefer the sites in the core of the nanowires, and therefore, N-doped SiC nanowires were found to fail as self-purifying materials.

One-dimensional systems are actively sought after also for their optical properties. Using the GW method, which is an accurate method for studying excited states, Bruno and coworkers (2007) demonstrated that optical properties of Si and Ge nanowires depend not only on the nanowire diameter but also on the orientation.

2D Structures: Graphene and Derivatives

Due to the remarkable ability of carbon to exist in different hybridization states, carbon-based materials display an unusually rich variety. Diamond, graphene, cage-like molecules and perhaps most notably carbon nanotubes are examples of the large selection of possibilities.

Graphene, which is a single layer of graphite, may be thought of as the building block of most of the allotropes listed above (► Fig. 27-9). Nanotubes are geometrically rolled up versions of graphene, and fullerenes can be formed by introducing topological defects (heptagons



■ Fig. 27-9

Graphene is a 2D building material for carbon materials of all other dimensionalities. It can be wrapped up into 0D buckyballs, rolled into 1D nanotubes, or stacked into 3D graphite (Reprinted with permission from Geim and Novoselov (2007). © (2007) by Nature Publishing Group)

and pentagons) into the perfect honeycomb lattice structure of graphene in order to introduce positive and negative curvature (Freitag 2008; Peres et al. 2006).

Regardless of the immense attention that graphene received in the theoretical literature, it wasn't until 2004 (Novoselov et al. 2004) that a single layer of graphene was isolated experimentally. Since two-dimensional crystals were proven to be unstable theoretically (Landau and Lifshitz 1980; Mermin 1968), the discovery of free-standing graphene came as a surprise (Meyer et al. 2007). This apparent discrepancy, however, was lifted when upon closer inspection, the isolated graphene sheets were not perfectly flat but had corrugations reaching up to 1 nm in size.

Since the discovery and isolation of graphene was achieved, many other materials were found to form two-dimensional structures. In this chapter, we give an overview of carbon-based two-dimensional materials including graphene, graphene nanoribbons, nanobelts, and strips in addition to two-dimensional structures of several other materials.

Graphene, Nanosheets, Nanoribbons, Nanobelts, Nanostrips

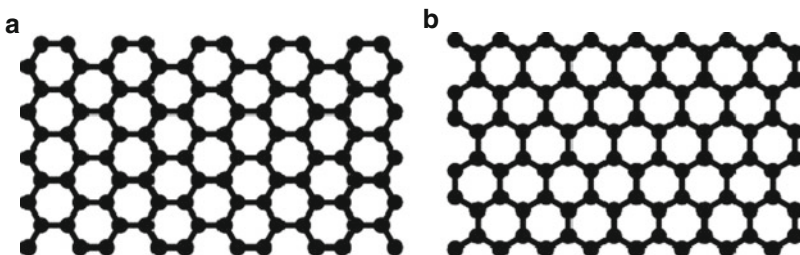
With the advent of several sophisticated experimental techniques, the two-dimensional confinement of graphene layers were further extended to one-dimensional in the form of *nanoribbons*. Nanoribbons are narrow strips of graphene that may exhibit quasi-metallic or semiconducting behavior depending on the geometry of their edges. Much like nanotubes, graphene nanoribbons (GNRs) are also termed *zigzag* or *armchair* based on the directionality of the bonds with respect to the long axis (see ► Fig. 27-10). Due to the dependence of their electronic properties on their geometry, it is important to control the morphology and crystallinity of these edges for practical purposes. It has been experimentally shown that (Jia et al. 2009) controlled formation of sharp zigzag and armchair edges in graphitic nanoribbons are possible by Joule heating. During Joule heating and electron beam irradiation, carbon atoms are vaporized, and subsequently sharp edges and step-edge arrays are stabilized, mostly with either zigzag- or armchair-edge configurations.

In addition to the edge geometry, the electronic properties, in particular the band gap, of nanoribbons also depend on their width (Han et al. 2007; Wu and Zeng 2008). The magnetic properties may also be severely altered upon reduction of size to a graphene fragment (Wang et al. 2008) which results in the emergence of giant spin moments.

Another path for controlling the electronic properties of nanoribbons is by an application of an external electric field or by chemical doping of the pristine samples. Half-metallicity, for instance, which has several applications in spintronics (Wu and Zeng 2008) may be introduced through functionalization with such species as H, COOH, OH, NO₂, NH₃, and CH₃ (Son et al. 2006).

Straight GNRs with zigzag, armchair, or mixed edges are proven to be semiconducting by the experiment. In addition, GNRs can be sculpted by attaching two segments together that are manufactured to make a 120 degree angle with each other thereby forming a *sawtooth-like* nanoribbon (► Fig. 27-11). The structure of a sawtooth-like GNR can be characterized by two integers (w, l). The first integer denotes the width of the nanoribbon, while the second integer describes its periodic length (Wu and Zeng 2008).

Stability is an important issue for a material which is intended to be used as a building block of device applications. Even though perfect two-dimensional crystals are proven to be unstable, graphene is found to be stabilized by corrugations in the third dimension. Understanding the effect of GNR width on the stability is therefore also a central issue for possible applications. Molecular dynamics computer simulations using empirical interatomic potentials predict that



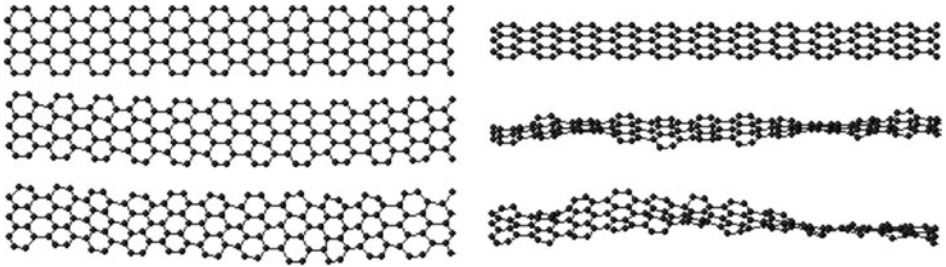
■ Fig. 27-10

(a) Armchair graphene ribbon model. (b) Zigzag graphene ribbon model



■ Fig. 27-11

The model structure of a sawtooth-like GNR (Adapted from Wu and Zeng 2008)



■ Fig. 27-12

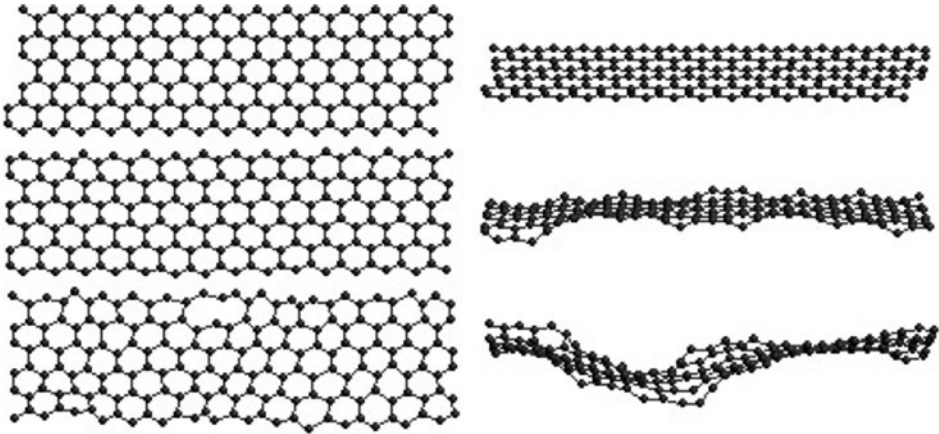
Armchair edged GNRs. *Left* column shows *top* view and *right* column shows tilted view. GNRs of width five hexagonal rings are shown. 1 K, 300 K, and final temperature images are given (Adapted from Dugan and Erkoc 2008)

structural stability of graphene nanoribbons show dependence on size (width) and edge orientation (Dugan and Erkoc 2008). ● *Figures 27-12* and ● *Fig. 27-13* show respectively the relaxed structures of armchair and zigzag edged GNRs with various widths.

In the recent nanoscale literature, a wealth of materials other than C have been identified, both theoretically and experimentally, as viable candidates for future use as two-dimensional devices.

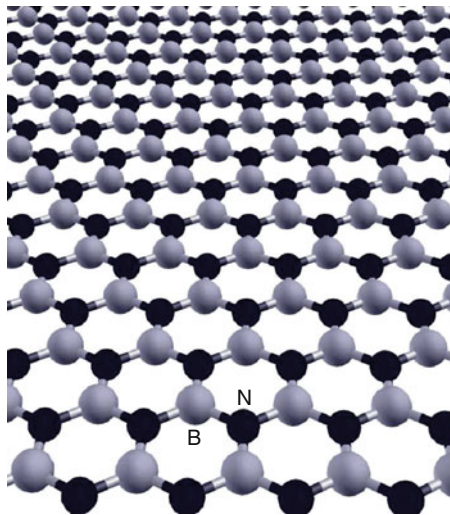
Boron nitride, for instance, having electronic properties that resemble carbon can exist in a hexagonal structure *h*-BN similar to the graphite layered geometry. Much like graphene sheets, BN sheets can be grown on more or less lattice-matched transition metal surfaces (Corso et al. 2004; Huda and Kleinman 2006). A model BN sheet is shown in ● *Fig. 27-14*.

BN, being a member of the III-V semiconductor family indicates the possibility of nanoribbons or nanobelts made of other semiconductor families. Indeed, several oxide and other II-VI family nanobelts have been discovered and reported (Pan et al. 2001) (ZnO, SnO₂, CdO, Ga₂O₃, PbO₂, ZnS, CdSe, and ZnSe). Some of the oxides in this family such as ZnO and SnO₂, owing to their polarity and crystal structure, deform in novel morphologies such as rings, springs, and spirals in order to bring together the positive and negative charges, counteracting the charge imbalance (Yang and Wang 2006). These structures comprise a versatile set of nanomaterials that are promising candidates for various applications such as sensors, resonators, and transducers.



■ Fig. 27-13

Zigzag edged GNRs. *Left column shows top view and right column shows tilted view. Ribbons of width five hexagonal rings are shown. 1 K, 300 K, and final temperature images are given (Adapted from Dugan and Erkoç 2008)*



■ Fig. 27-14

The geometric structure of BN sheet (Adapted from Venkataraman et al. 2009)

Nanobelts, a term coined by researchers working on these structures (Wang 2004), are described as nanowires with not only a well-defined growth direction but also well-defined top, bottom and side edges and cross-section. The nanobelt structures are usually obtained from functional oxides, which are semiconductor materials, such as ZnO, Ga₂O₃, t-SnO₂, o-SnO₂, In₂O₃, CdO, and PbO₂. Pure metal nanobelt structures are also possible, Zn is one of the metals that form fine nanobelt structures (Wang 2004). ZnO, being one of the most versatile materials in nanoscale research alongside with carbon and BN, has once again been investigated at

great depth in the context of nanobelts (Kulkarni et al. 2005; Wang 2004). Molecular dynamics computer simulations using empirical interatomic potentials (Kulkarni et al. 2005) reveal that ZnO nanobelts display properties that depend on their size and orientation. Depending on the growth direction, ZnO nanobelts may exhibit an interesting shell structure or a simple surface reconstruction.

Nanostrips are similar to nanobelts, they are used with the same meaning with nanobelts. All these nanostructures (ribbons, belts, strips) are ideal materials for building nano-sized devices and sensors (Lin et al. 2009).

In addition to the materials mentioned above, recent theoretical studies have proposed a wealth of two-dimensional structures that are composed of less common materials. One such example is the recently proposed B₂C graphene (Wu et al. 2009). The optimized B₂C graphene structure is displayed in **Fig. 27-15**. Two neighboring CB₄ motifs share two common boron atoms, giving rise to a hexagon and a rhombus. The mean B–C and B–B bond length is 1.557 and 1.685 Å, respectively. The sheet is slightly corrugated with a distance of only ~0.085 Å. The corrugation is a result of an excess of 2p electrons normal to the sheet relative to the gas-phase CB₄ molecule.

The quasi-one-dimensional B₂C nanoribbons are finite-size graphene with parallel edges. The width of the B₂C nanoribbon is defined by the number of C atoms normal to the long-axis of the ribbon. As shown in **Fig. 27-15**, type I and II B₂C nanoribbons are displayed. The dangling bonds at the edges of B₂C nanoribbons can be passivated by either H atoms or CH groups.

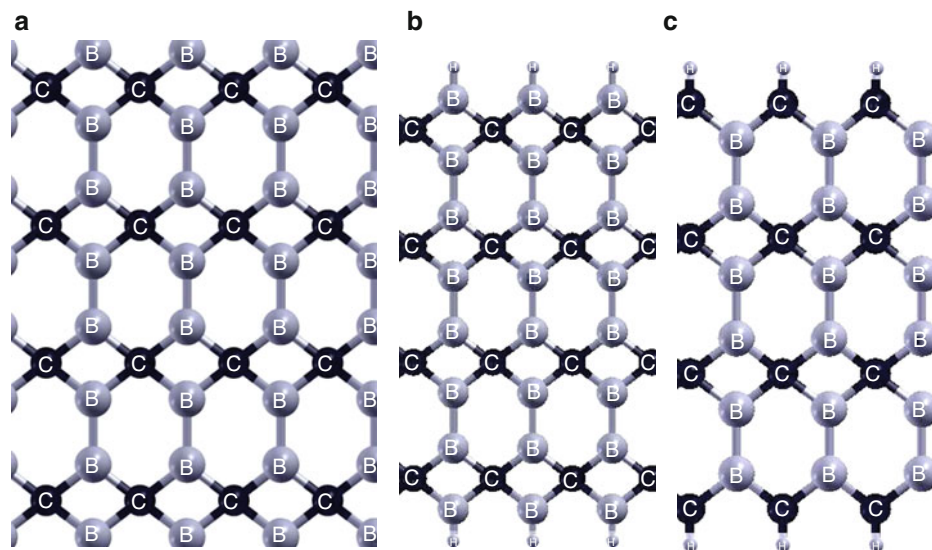
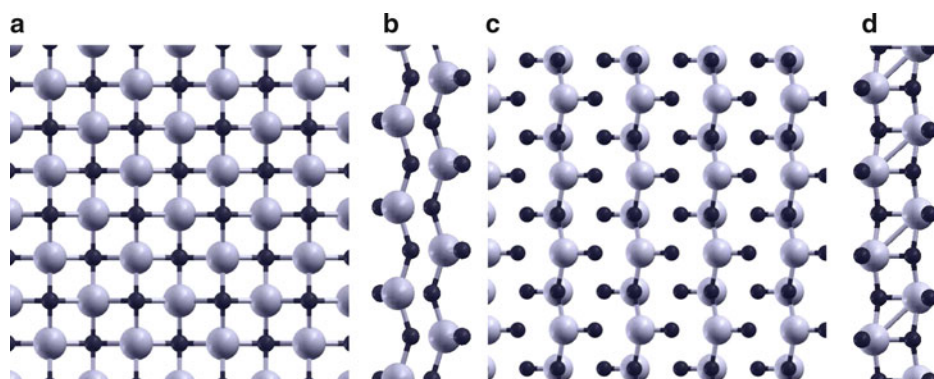


Fig. 27-15

(a) A C_{2v}-CB₄ motif structure. Each carbon atom is bonded with four boron atoms. Optimized structures of two types B₂C nanoribbons with two different edge configurations, referred as type I (b) and type II (c) (Adapted from Wu et al. 2009)

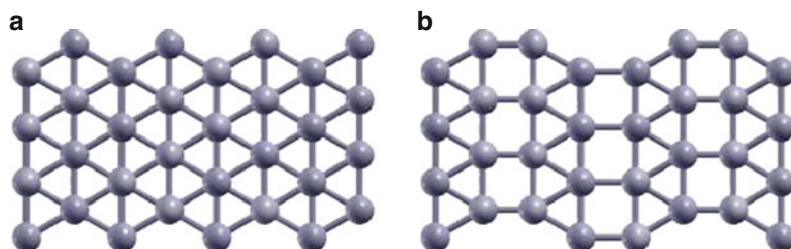
TiO₂ with its uses in solar cell applications and surface catalysis has received much attention both theoretically and experimentally. Its nanostructures are of equal interest to technology due to their chemical inertness, endurance, strong oxidizing power, large surface area, high photocatalytic activity, non-toxicity, and low production cost. The titania nanostructures are constructed by “cutting” of TiO₂ monolayers into nanostrips and by rolling them into cylindrical nanotubes or nanorolls (Enyashin and Seifert 2005). There are two different topological nanostrip models constructed from titania. One model is obtained from (101) surface of titania, called as anatase layer, and the second model is obtained from (010) surface of titania, called as lepidocrocite layer. A view of the structures of (101) and (010) TiO₂ layers are shown in ► Fig. 27-16. By rolling of these strips various nanostructures can be generated, such as nanotubes and nanospirals (nanorolls) (Enyashin and Seifert 2005).

Non-carbon elemental sheet structures have also been investigated. Lau et al. (2006) proposed four possible configuration models for the boron sheet. According to this study, the flat form, denoted {1212}, seen in ► Fig. 27-17 is a triangular network, while the buckled {1212}^b and pair-buckled {1212}^{pb} configurations include chain-wise and pair-wise out-of-plane displacements. Finally, a reconstructed {1221} configuration is investigated with inversion symmetry in the unit cell. It can be considered as a triangular-square-triangular unit network.



■ Fig. 27-16

Monolayers of TiO₂ in anatase (*top* (a) and *side* (b)) and lepidocrocite polymorphs (*top* (c) and *side* (d))



■ Fig. 27-17

Idealized 1212 (a) and reconstructed 1221. (b) Boron sheets

The DFT calculations reveal (Lau et al. 2006) that the reconstructed $\{1221\}$ configuration is the most stable configuration by 0.23 eV/atom relative to the idealized $\{1212\}$ configuration. Both the $\{1212\}^b$ and $\{1212\}^{bb}$ configurations tend to converge to the idealized $\{1212\}$ configuration when relaxed during the geometry optimization.

Electronic and Mechanical Properties

Graphene has a unique and curious band structure which can be approximated by a double cone close to the six Fermi points at the corners of the Brillouin zone (see  Fig. 27-18). Commonly referred to as Dirac electrons, the conduction electrons follow a linear energy-momentum dispersion and have a rather large velocity.

The conduction in graphene is enabled by the delocalized π -electrons above and below the plane. Due to their relative detachment from the tightly-knit planar network these electrons are free to move along the graphene sheet with rather high mobility. This is of course a rather desirable property for devices used in electronics (Li et al. 2008b).

A good yet simple method for understanding the band structure of graphene is the tight-binding formalism (Neto et al. 2009). Graphene is made out of carbon atoms arranged in hexagonal structure, as shown in  Fig. 27-19. The structure can be seen as a triangular lattice with a basis of two atoms per unit cell. The lattice vectors can be written as

$$\mathbf{a}_1 = \frac{a}{2}(3, \sqrt{3}), \quad \mathbf{a}_2 = \frac{a}{2}(3, -\sqrt{3}),$$

where $a \sim 1.42 \text{ \AA}$, is the carbon-carbon distance. The reciprocal-lattice vectors are given by

$$\mathbf{b}_1 = \frac{2\pi}{3a}(1, \sqrt{3}), \quad \mathbf{b}_2 = \frac{2\pi}{3a}(1, -\sqrt{3}),$$

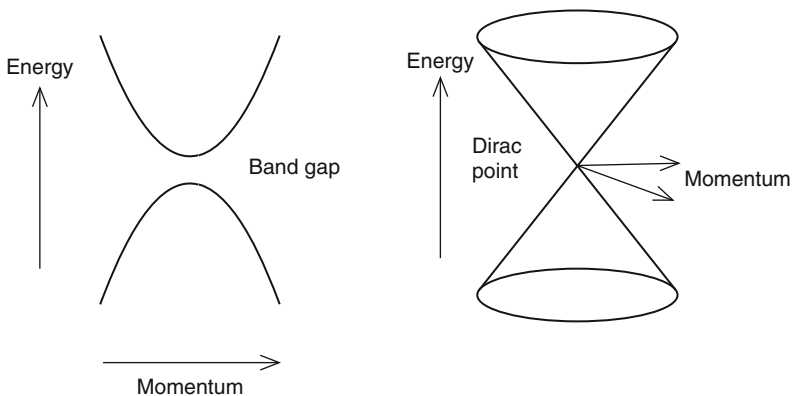
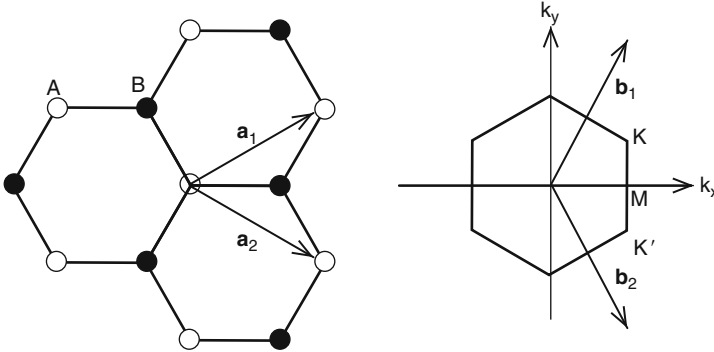


 Fig. 27-18

The band structure of a representative three-dimensional solid (*left*) is parabolic, with a band gap between the lower-energy valence band and the higher-energy conduction band. The energy bands of 2D graphene (*right*) are smooth-sided cones, which meet at the Dirac point



■ Fig. 27-19

Graphene lattice and its Brillouin zone. *Left:* lattice structure of graphene, made out of two interpenetrating triangular lattices (a_1 and a_2 are the lattice unit vectors). *Right:* corresponding Brillouin zone. The Dirac cones are located at the K and K' points

The two points K and K' at the corners of the graphene Brillouin zone (BZ) are named Dirac points. Their positions in momentum space are given by

$$\mathbf{K} = \left(\frac{2\pi}{3a}, \frac{2\pi}{3\sqrt{3}a} \right), \quad \mathbf{K}' = \left(\frac{2\pi}{3a}, -\frac{2\pi}{3\sqrt{3}a} \right).$$

The tight-binding Hamiltonian for electrons in graphene, considering that electrons can hop to both nearest- and next-nearest-neighbor atoms, has the form (in units $\hbar = 1$)

$$H = -t \sum_{\langle i,j \rangle, \sigma} (a_{\sigma,i}^\dagger b_{\sigma,j} + H.c.) - t' \sum_{\langle\langle i,j \rangle\rangle, \sigma} (a_{\sigma,i}^\dagger a_{\sigma,j} + b_{\sigma,i}^\dagger b_{\sigma,j} + H.c.), \quad (27.6)$$

where $a_{i,\sigma}$ ($a_{i,\sigma}^\dagger$) annihilates (creates) an electron with spin σ ($\sigma = \uparrow, \downarrow$) on site \mathbf{R}_i on sublattice A (an equivalent definition is used for sublattice B), t (~ 2.8 eV) is the nearest-neighbor hopping energy (hopping between different sublattices), and t' (~ 0.1 eV) is the next nearest-neighbor hopping energy (hopping in the same sublattice). The Hamiltonian in \blacktriangleright Eq. 27.7 is solved at various momenta and the energy bands are obtained as follows:

$$E_{\pm}(\mathbf{k}) = \pm t \sqrt{3 + f(\mathbf{k})} - t' f(\mathbf{k}) \quad (27.7)$$

with

$$f(\mathbf{k}) = 2 \cos(\sqrt{3}k_y a) + 4 \cos\left(\frac{\sqrt{3}}{2}k_y a\right) \cos\left(\frac{3}{2}k_x a\right), \quad (27.8)$$

where the plus sign applies to the upper (π^*) and the minus sign the lower (π) band.

As illustrated by this simple model, graphene is a semimetal or a zero-gap semiconductor. At low temperatures it does not possess superconducting properties; however, as demonstrated by Pathak et al. (2008) using variational Monte Carlo, there is a possibility that doped graphene may superconduct.

The graphene nanoribbons (GNRs) discussed in the previous sections may also be modeled rather easily using the tight-binding formalism taking as the basis the usual Schrödinger's

equation (Ezawa 2006) or the massless particle Dirac equation (Sasaki et al. 2006). These models predict that armchair GNRs can be either metallic or semiconducting depending on their widths, and that zigzag GNRs with zigzag shaped edges are metallic regardless of the width.

The edges of GNRs are also suitable sites for chemical functionalization (Wang et al. 2007). Due to the existence of dangling bonds at the edges, the electronic properties of GNRs may be controlled by modifying these bonds by addition of other species.

The results of first-principle calculations using linear combination of atomic orbital density functional theory (DFT) method predict that the electronic band structures and band gaps of the GNRs show a dependence on the edge structure of the nanoribbons (Wu and Zeng 2008). Clearly, the electronic band structures are sensitive to the edge structure of the nanoribbons. All straight GNRs are semiconducting. Two distinct features can be seen concerning the band gap. The band gap of GNR with zigzag edges slightly decreases with increasing the width w , while that of GNR with armchair edges varies periodically as a function of w .

Like the straight GNRs, the calculated electronic band structures of the sawtooth-like GNRs (see  Fig. 27-20) also show semiconducting characteristics with direct band gap. More interestingly, even though the sawtooth-like GNRs have zigzag edges, their band gaps show similar oscillatory behavior as those of straight GNRs with armchair edges, which depend on the width w . However, for most nanoribbons, their band gap reduces monotonically with increasing periodic length l . The band gaps of nanoribbons with $w = 1, 2, \text{ or } 4$ reduce much rapidly, whereas those of nanoribbons with $w = 3 \text{ or } 5$ reduce gradually.

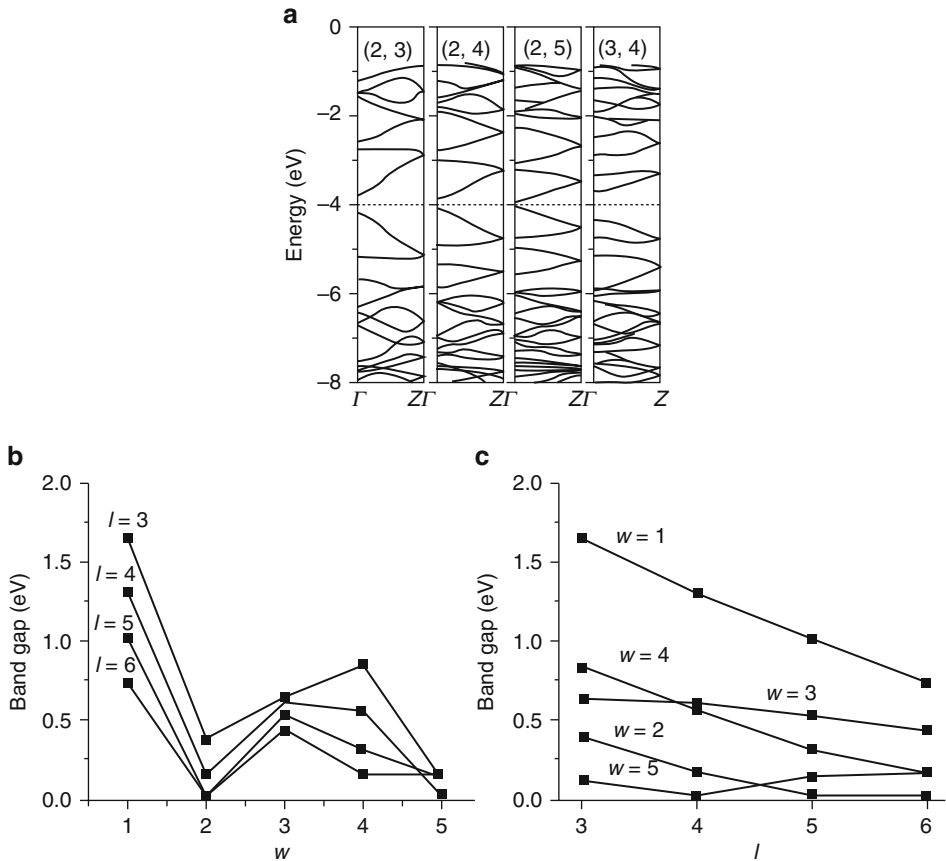
For $(2, l)$ sawtooth-like nanoribbons, the band gap approaches zero rapidly as the l increases (Wu and Zeng 2008). These results show that the band gaps of the sawtooth-like GNRs are much more sensitive to their geometric structures, which is an opportunity for tuning the band gap.

Quantization of electric conductance under the action of an external magnetic field displays a rather interesting trend for GNRs. In the exhaustive tight-binding study conducted by Peres et al. (2006), the number of plateaus in the quantized conductance was found to be even in armchair GNTs while the same number is odd for the zigzag edge.

Rosales et al. (2008) investigated theoretically the effects of side-attached one-dimensional chains of hexagons pinned at the edges of the GNRs. These one-dimensional chains could be useful to simulate, qualitatively, the effects on the electronic transport of GNRs when benzene-based organic molecules are attached to the edges of the ribbons. They propose a simple scheme to reveal the main electronic properties and the changes in the conductance of such decorated planar structures. For simplicity, they consider armchair and zigzag nanoribbons and linear poly-aromatic hydrocarbons (LPHC) and poly(paraphenylene), as the organic molecules. The attached molecules are simulated by simple one-dimensional carbon hexagonal structures connected to the GNRs.

These nanostructures are described using a single-band tight-binding Hamiltonian and their electronic conductance and density of states are calculated within the Green's function formalism based on real-space renormalization techniques (Rosales et al. 2008).

As revealed by the theoretical analysis conducted by Nakabayashi et al., GNRs are a solution to the difficulty of producing an effective graphene switch for turning off the current. Zigzag nanotubes due to their peculiar band structures may be utilized for better current control rather than graphene. A single layer of graphene has no bandgap, which makes it difficult to control current. However, Nakabayashi et al. (2009) found that when a sheet of graphene was in the form of nanoribbons just a few nanometers wide, its electronic structure changed so that currents could be controlled in radically different ways in comparison to conventional semiconductor devices. Nakabayashi et al. (2009) showed that when a nanoribbon was cut so that

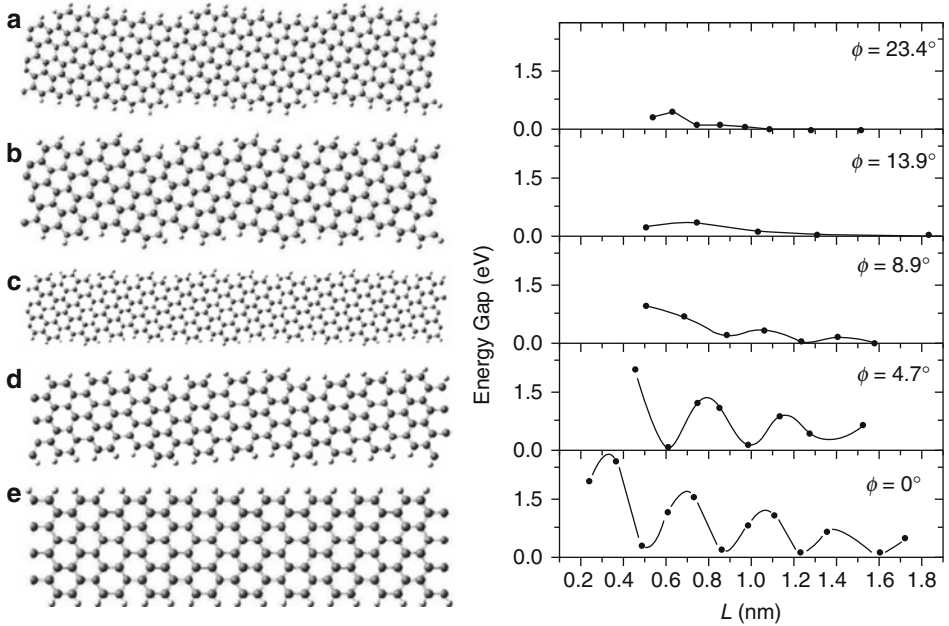


■ Fig. 27-20

(a) The electronic band structures of several sawtooth-like GNRs with various w and l . The band gaps versus (b) the width w and (c) the periodic length l (Reprinted with permission from Wu and Zeng (2008). © (2008) by Springer)

its edges formed a zigzag structure with an even number of zigzag chains across its width, and an electrostatic barrier potential applied along part of its length, then it behaved as a so-called band-selective filter, preferentially scattering charges into either even or odd numbered bands of its electronic structure depending on the potential. And when two such filters with different potentials were connected in series, they showed it should be possible to completely shut off the flow of current through the nanoribbons.

Tight-binding studies have revealed countless interesting electronic properties regarding GNRs. GNRs, much like single-walled carbon nanotubes, can display metallic or semiconducting properties depending on their orientation and width. Similar to armchair nanotubes, zigzag ribbons are all metallic and may have magnetic properties. Bare and H-terminated ribbons, as studied by Barone et al. may show such effects as gap oscillations which make them a viable choice for possible band structure engineering applications. The results of this study, which is a careful investigation of GNRs of several orientations, widths and terminations are displayed



■ Fig. 27-21

Left: A representative set of semiconducting hydrogen-terminated GNRs, created by “unfolding” and “cutting” different types of CNTs. (a) A GNR with a chiral angle of $\phi = 23.4^\circ$ created by unfolding and cutting a C(6,4). (b) A GNR with a chiral angle of $\phi = 13.9^\circ$ created by unfolding and cutting a C(6,2). (c) A GNR with a chiral angle of $\phi = 8.9^\circ$ created by unfolding and cutting a C(20,4). (d) A GNR with a chiral angle of $\phi = 4.7^\circ$ created by unfolding and cutting a C(10,1). (e) An armchair GNR ($\phi = 0^\circ$) created by unfolding and cutting a zigzag CNT. *Right:* Dependence of the band gap on the width of hydrogen passivated chiral GNRs. The different panels correspond to the different CNRs presented in Left. (Reprinted with permission from Barone et al. (2006). © (2006) by the American Chemical Society)

in ● Fig. 27-21 along with the details of the models used and the band gap profiles of the corresponding models.

GNRs have localized edge states located near the Fermi level. By terminating the edges with different species, one can change the character of these states and consequently the properties of GNRs. In fact, a first-principles calculation within spin-unrestricted local-density functional formalism on zigzag-edge graphene nanostrips terminated with hydrogen and oxygen atoms as well as hydroxyl and imine groups show that these different species have a significant impact on the electronic structure of these strips near the Fermi level (Gunlycke et al. 2007). Zigzag-edge nanostrips terminated with hydrogen atoms or hydroxyl groups exhibit spin polarization, while the nanostrips terminated with oxygen or imine groups are unpolarized. These differences of course result in very different conductance characteristics for these systems.

In further support of the aforementioned evidence Zhang and Yang (2009) confirmed in their linear combination of atomic orbitals (LCAO) tight-binding study that H-terminated armchair GNTs exhibit size dependence in their conductance properties.

On the other hand, ZnO nanoribbons show different characteristics from that of carbon nanoribbons. ZnO nanoribbons grown along the [0001] direction can form two different planar monolayer, zigzag and armchair ribbons. First principles calculations of zinc oxide nanoribbons show that the stability of armchair edge structures is greater than the zigzag edge configurations. Furthermore, single layered armchair ribbons are semiconductors, whereas the zigzag counterparts are metallic (Botello-Mendez et al. 2007). An effect that is not present in purely carbon-based systems is the presence of two differently charged species offering different edge configurations. For the zigzag ZnO ribbons, for instance, the exposed atoms are oxygen atoms while the hidden are zinc. The opposite edge has the inverse structure. The armchair ribbons are characterized by a Zn-O pair at the outer edge and another pair at the inner edge. After relaxation, the far edge oxygen ions tend to shift outward on both sides of the ribbon. As in the case of graphene materials, understanding the effects of edge-dimensional variation on band gap energies will provide the new insights into the fundamental principle of architecture design of nanodevices fabricated with ZnO nanostructured materials. A simple tight-binding model can be used to investigate the electronic properties of nonpolar ZnO nanobelts following the procedure described below.

Consider a simplified unit cell model (see  Fig. 27-22) along the nanobelt growth z direction with Zn and O in the xy plane. This is the actual case for the ultrathin ZnO film oriented along the [001] direction.

In this case, the tight-binding Hamiltonian is given by (Yang and Wang 2006):

$$H = \sum_{r \in A} \varepsilon_r a_r^\dagger a_r + \sum_{r \in B} \varepsilon_r b_r^\dagger b_r + \sum_{r \in A, B} \sum_{i=1,2,\dots} (\tau_{r,i} a_r^\dagger b_{r+S_i} + \tau_{i,r}^* b_r^\dagger a_{r+S_i}),$$

where operators a_r^\dagger (a_r) and b_r^\dagger (b_r) create (annihilate) a state at sites A (for Zn) and B (for O) at their coordinates r , respectively. ε denotes the on-site self-interaction energy, whereas τ is the interatomic coupling term. Similarly, the wave functions for Zn and O at their respective lattice sites can be written as a linear combination of Bloch waves along the z direction and standing waves along x and y as the following (Yang and Wang 2006),

$$|\text{Zn}, k_x, k_y \rangle = \sum_{m_x=1}^{M_x} \sum_{m_y=1}^{M_y} \sum_{z_m} c_p e^{ik_z z_m} \sin(k_x m_x a) \sin(k_y m_y b) a_{m_x m_y}^\dagger |0 \rangle$$

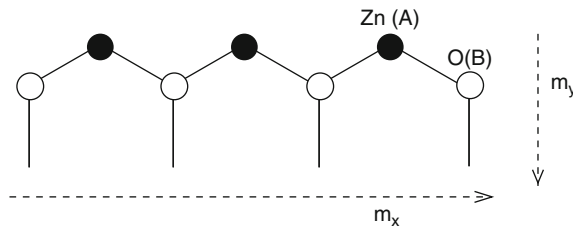


 Fig. 27-22

Schematic illustration showing a tight binding unit cell for a ZnO nanobelt (Adapted from Yang and Wang 2006)

$$|O, k_x, k_y \rangle = \sum_{n_x=1}^{N_x} \sum_{n_y=1}^{N_y} \sum_{z_n} c_p e^{ik_z z_n} \sin(k_x n_x a) \sin(k_y n_y b) a_{n_x n_y}^+ |0 \rangle$$

in which lattice vectors a and b are as defined in [Fig. 27-19](#) and c_p and c_q are coefficients.

To simplify the model, one may consider only the coupling term between the nearest neighboring sites. In this case, on the same xy plane, the O-sites take the following coordinates around a Zn center: $n_x = m_x - 1, m_x$ and $m_x + 1$; with $n_y = m_y - 1, m_y$ and $m_y + 1$ in correspondence. Along the yz plane, there exist two O atoms that directly interact with the center Zn with $z_n = z_m \pm c$, respectively (Yang and Wang 2006).

In addition to the conventional strip-like geometry, other configurations based on GNRs have also been proposed as a part of a search for favorable transport properties. Various graphene nanojunctions based on the GNRs have been studied, such as L-shaped, Z-shaped, and T-shaped GRN junctions (Areshkin et al. 2007; Chen et al. 2008; Jayasekera and Mintmire 2007). Of particular interest is the hybrid junctions which are mixtures of armchair and zigzag GNRs. Some studies have shown that the transport properties of these hybrid GNR junctions are very sensitive to the details of the junction region (Xie et al. 2009). A model calculation based on tight-binding and Green's function methods for L-shaped GNRs show that the corner geometry of the L-shaped junction has great influence on the electron transport around the Fermi energy (Xie et al. 2009). The L-shaped GNR models considered are shown in [Fig. 27-23](#). The calculated conductance plots as a function of electron energy are shown in [Fig. 27-24](#). Interestingly the results reveal that the corner is the decisive factor for the electronic properties of these junctions. As more carbon atoms are added to the inner side of the corner the junction moves from being metal to a semiconductor, developing a band gap.

Carbon nanoribbons have also interesting mechanical properties. For instance, Raman spectra show a remarkable dependence on ribbon width (W) (Zhou and Dong 2008). For the

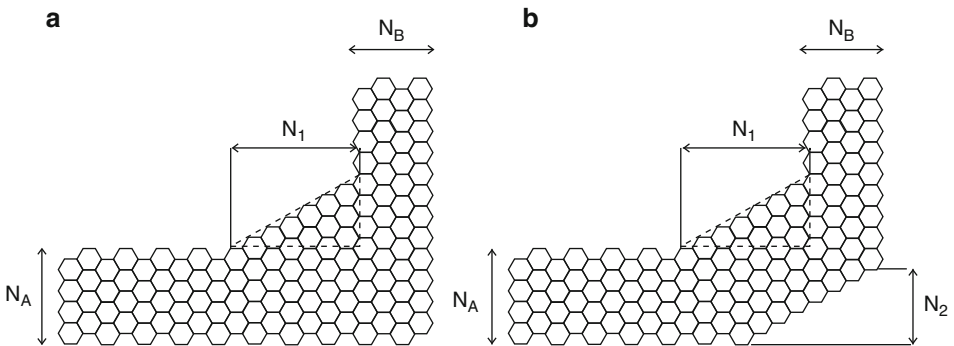
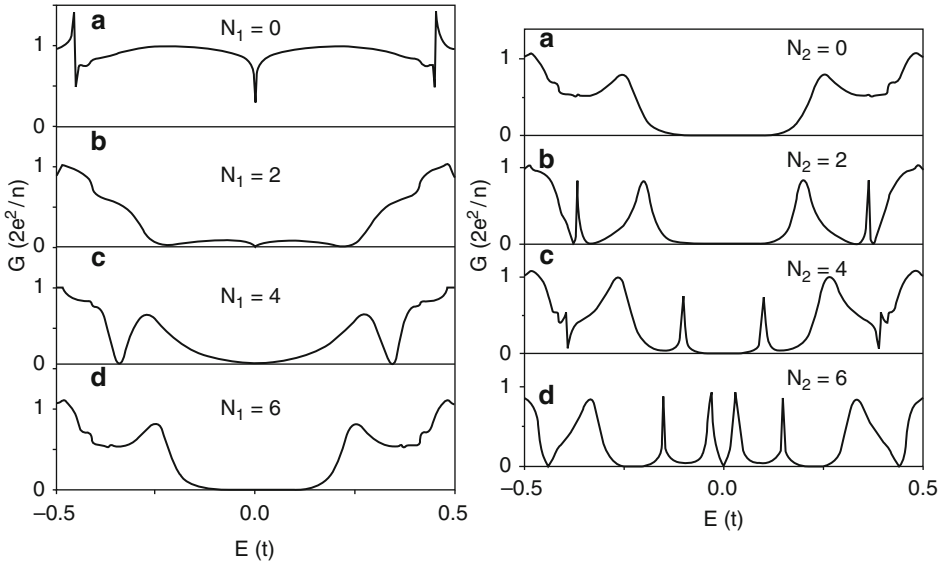


Fig. 27-23

(a) A deformed LGNR (called LGNR1) where a triangle graphene flake (in the dashed-line triangle) is connected to the inside corner of a standard right-angle LGNR. (b) A deformed LGNR (called LGNR2) in which a triangle graphene flake is cut from the outside corner of LGNR1 in (a). N_A and N_Z represent the widths of the semi-infinite AGNR and ZGNR, respectively; N_1 represents the side length of added triangle flake, while N_2 represents the side length of cut triangle flake (Adapted from Xie et al. 2009)



■ Fig. 27-24

Left: The conductance as a function of electron energy for the LGNR1 in [Fig. 27-23a](#) with different N_1 . Other parameters are $N_A = 11$ and $N_Z = 7$. **Right:** The conductance as a function of electron energy for the LGNR2 in [Fig. 27-23b](#) with $N_1 = 6$ and different N_2 . Other parameters are $N_A = 11$ and $N_Z = 7$ (Reprinted with permission from Xie et al. (2009). © (2009) by Elsevier)

GNRs whose widths are larger than 25 \AA , the radial breathing-like mode (RBLM) frequencies follow the $1/W$ rule:

$$\omega = 3086.97 \times \frac{1}{W} + 1.08 \text{ in } 1/\text{cm}.$$

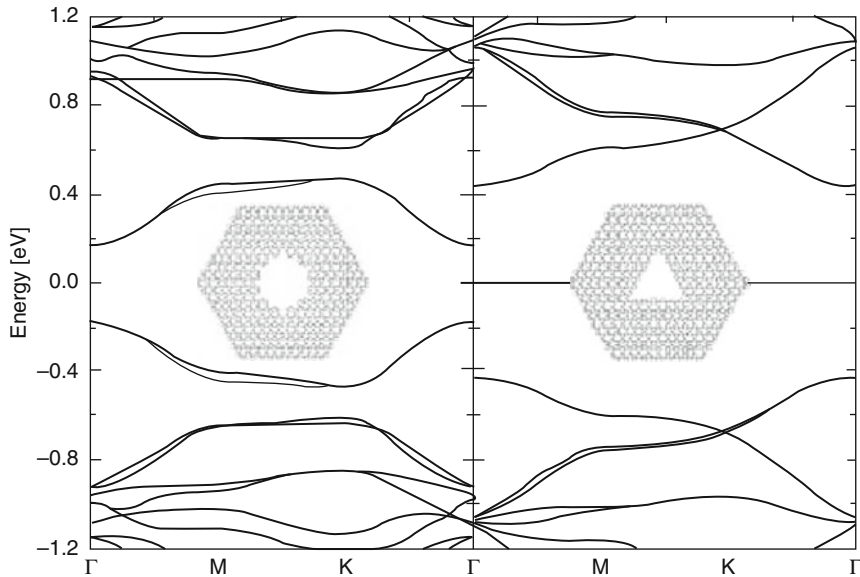
But for the narrow GNRs whose widths are less than 25 \AA , their RBLM frequencies follow the $1/\sqrt{W}$ rule:

$$\omega = 1407.81 \times \frac{1}{\sqrt{W}} + 164.38 \text{ in } 1/\text{cm}.$$

A unified fitting function has been proposed (Zhou and Dong 2008), which can be suitable for all the GNRs:

$$\omega = 1584.24 \times \frac{1}{W} + 351.98 \times \frac{1}{\sqrt{W}} - 10.0 \text{ in } 1/\text{cm}.$$

Another interesting application of graphene is the antidot lattices. Antidot lattices are triangular arrangements of holes in an otherwise perfect graphene sheet. In each hexagonal unit cell of the lattice, a circular hole is introduced whose radius R can be adjusted along with the length of the hexagonal unit cell, L . Previously known applications of antidot lattices involve semiconductor lattices, while in a recent publication the possibility of creating antidot structures on graphene using e-beam lithography has been reported (Pedersen et al. 2008). The antidot lattice causes graphene to become a semiconductor, introducing a tuning parameter which is the dot size and shape. In addition spin qubit states can be formed in the antidot lattice by manipulating the antidot arrangement. Pedersen et al. (2008) demonstrated that the hole shape plays a



■ Fig. 27-25

Band structures of a $\{10, 3\}$ antidot lattice and similar structure having a triangular hole with zigzag edges. Note the dispersion less band at 0 eV in the triangular case (Reprinted with permission from Pedersen et al. (2008). © (2008) by the American Physical Society)

crucial role in determining the electronic structure. A triangular hole instead of a circular hole results in the appearance of a metallic state at the Fermi level. The different band structures are illustrated in ● Fig. 27-25.

Magnetic and Optical Properties

Lower-dimensional systems are expected to show electronic, magnetic, and optical properties that are not observed in their bulk counterparts. In two-dimensional structures, the inherent or emergent magnetic properties depend on many factors including shape, size, and the interaction between subregions (Jensen and Pastor 2003).

GNRs are a typical example of emergent and controllable magnetic systems. Spin-polarized first-principles calculations by Gorjizadeh et al. (2008) have shown that doping GNRs with 3d transition metals result in the appearance of FM or AFM states. In particular Cr and Co provide a large magnetic moment and doping with Fe or Mn at low densities yields half-metallic ribbons.

As discussed in the work by Enoki and Takai, as the dimension of the system decreases, the contribution coming from the edge states increases in proportion (Enoki and Takai 2009). The localized edge states in GNR, which are dispersionless states that appear at the Fermi level give rise to interesting magnetic properties.

From the applications point of view the magnetic properties of graphene nanoribbons are more interesting and studied both experimentally and theoretically. Particularly quasi 1D GNRs have magnetic properties depending on their size and symmetry. These are edge states

of nanoribbons with opposite spin polarization and band gaps varying with the width of the ribbon (Topsakal et al. 2008).

Using first-principles plane wave calculations within the DFT method Topsakal et al. (2008) predict that in addition to edge states electronic and magnetic properties of graphene nanoribbons can also be affected by defect-induced states. In particular, when H-saturated holes are introduced into the GNT, the band structure is modified dramatically altering in return the electronic and magnetic properties. Similarly, vacancies and divacancies induce metallization and magnetization in non-magnetic semiconducting nanoribbons due to the spin-polarization of local defect states. Antiferromagnetic ground state of semiconducting zigzag ribbons can change to ferrimagnetic state upon creation of vacancy defects. In this study, the changes in electronic properties are studied as a function of the location and the geometry of the vacancies in different types of armchair GNRs. Due to the spin polarization of localized states and their interaction with edge states, magnetization may be introduced into the GNRs. Some of the representative results of this work are displayed in  Fig. 27-26.

Not only armchair, but also zigzag nanoribbons are strongly affected by defects due to single and multiple vacancies (Topsakal et al. 2008). When coupled with the magnetic edge states of the zigzag nanoribbons the vacancy defect brings about additional changes. The magnetic state and energy band structure of these ribbons depend on the type and geometry of the defects. In a ZGNR(14;8) a single vacancy formation energy is lowered by 0.53 eV when the defect is situated at the edge rather than at the center of the ribbon. Furthermore, two defects associated

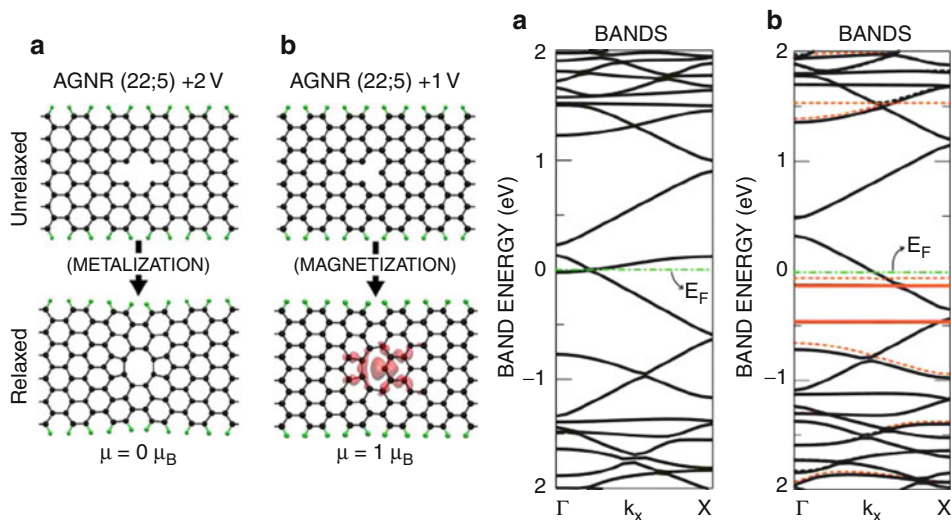


 Fig. 27-26

(a) Metallization of the semiconducting AGNR(22) by the formation of divacancies with repeat period of $l = 5$. (b) Magnetization of the non-magnetic AGNR(22) by a defect due to the single carbon atom vacancy with the same repeat periodicity. Iso-surfaces around the vacancy correspond to the difference of the total charge density of different spin directions. Solid (blue) and dashed (red) lines are for spin-up and spin-down bands; solid (black) lines are nonmagnetic bands (Reprinted with permission from Topsakal et al. (2008). © (2008) by the American Physical Society)

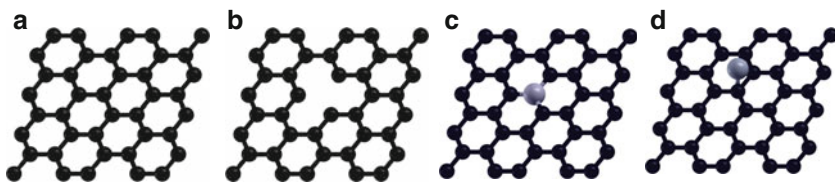
with two separated vacancy and a defect associated with a relaxed divacancy exhibit similar behavior (Topsakal et al. 2008).

On the other hand, Pisani et al. (2007) investigated theoretically the electronic and magnetic properties of zigzag graphene nanoribbons by performing first principles calculations within DFT formalism. They predict that the electronic structure of graphene ribbons with zigzag edges is unstable with respect to magnetic polarization of the edge states.

As can be seen from the model calculations of Topsakal et al. (2008, 2007), the energy band gaps and magnetic states of graphene nanoribbons can be modified by defects due to single or multiple vacancies. Electronic and magnetic properties of finite length graphene nanoribbons also show similar behavior as infinite length nanoribbons. Finite length ribbons are usually referred to as *graphene quantum dots* (GQD). Tang et al. (2008) investigated theoretically the electronic and magnetic properties of a square graphene quantum dot. Electronic eigen-states of a GQD terminated by both zigzag and armchair edges are derived in the theoretical framework of the Dirac equation. They find that the Dirac equation can determine the eigen-energy spectrum of a GQD with good accuracy. By using the Hartree-Fock mean field approach, they studied the size dependence of the magnetic properties of GQDs. They find that there exists a critical width between the two zigzag edges for the onset of the stable magnetic ordering. On the other hand, when such a width increases further, the magnetic ground state energy of a charge neutral GQD tends to a saturated value (Tang et al. 2008).

Magnetic properties of graphene show a sensitive dependence on single atom defects; defect concentration and packing play an important role in magnetism. Singh and Kroll (2009) investigated the magnetism in graphene due to single-atom defects by using spin-polarized density functional theory calculations. Interestingly, they find that while the magnetic moment per defect due to substitutional atoms and vacancies depend on the defect density, it is independent of defect density for adatoms. The graphene sheet with B adatoms is found to be nonmagnetic, but with C and N adatoms it is magnetic. The adatom defects cause a distortion of the graphene sheet in their vicinity. The distortion in graphene due to C and N adatoms is significant, while the distortion due to B adatoms is very small. The vacancy and substitutional atom (B, N) defects in graphene are planar in the sense that there is in-plane displacement of C atoms near the vacancy and substitutional defects. Upon relaxation the displacement of C atoms and the formation of pentagons near the vacancy site due to Jahn–Teller distortion depends upon the density and packing geometry of vacancies (Singh and Kroll 2009). The defect models considered by Singh and Kroll are shown in [Fig. 27-27](#).

The optical absorption coefficient is one of the most important quantities in solids and is closely related to the electronic band structure. The Kubo formula-based calculations of



■ Fig. 27-27

The model samples of (a) ideal graphene, (b) graphene with one atom vacancy, (c) graphene with one substitutional atom and (d) graphene with one adatom defect (Adapted from Singh and Kroll 2009)

Zhang et al. indicate that at high frequencies, the optical spectrum of graphene is highly anisotropic (Zhang et al. 2008). It has also been shown that the weak optical response in graphene nanoribbons can be significantly enhanced in an applied magnetic field (Liu et al. 2008).

Another effect important for determining the optical properties of graphene-related materials is spin-orbit coupling. Although spin-orbit coupling is negligible at high frequencies, it is found to have a significant enhancing effect on the optical absorption at lower frequencies as shown in a direct solution of the spin-orbit Hamiltonian in the effective mass approximation by Wright et al. (2009).

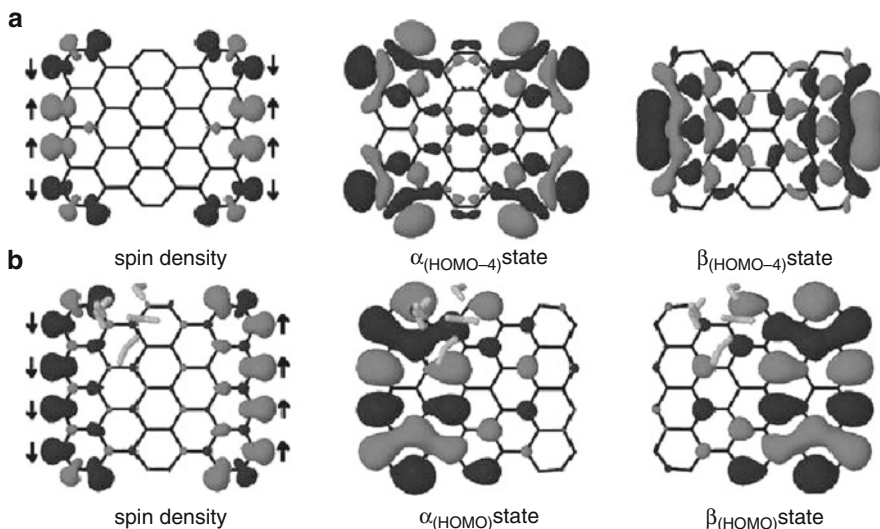
Adsorption Phenomena

Adsorption of adatoms on graphene and/or graphene nanoribbons play an important role in functionalizing graphene materials for various device applications, such as gas sensors and spin-valves. Transition metal (TM) atom decorated graphene shows different magnetic properties depending on the concentration and the species of TM atoms. There are several coverage models, such as one TM atom adsorbed on either (2×2) or (4×4) unit cells on only one side as well as on both sides, namely, above and below the graphene. Sevincli et al. (2008) investigated the possible adsorption sites of TM atoms on graphene and GNR. The geometrical configurations of the structures they considered include bridge (over a C–C bond), atop (on top of a C atom) and on center (over the center of a hexagon) adsorption sites for both perfect graphene and for AGNR of various widths N_a .

In relation to another very important application, doping of transition elements was found to increase the hydrogen storage properties of materials (Shevlin and Guo 2006). Especially nickel and rhodium are widely used in the hydrogenation reaction and also in the synthesis of BN sheets. Considering the potential application of Ni and Rh nanoparticles in hydrogen storage and in catalysis, Venkataramanan et al. (2009) investigated the interaction of Ni and Rh atom on the BN sheets through first-principles calculations. They also analyzed the interaction between hydrogen molecules and the metal atoms adsorbed on the BN sheets, which might be useful to maximize the hydrogen storage capacity.

Hydrogen adsorption studies over the metal doped BN sheets shows that both Ni and Rh atoms can hold three hydrogen molecules. In the case of Ni doped BN sheet all three hydrogen molecules are chemically bound and are intact. In the case of Rh doped BN sheets, the first hydrogen molecule dissociates and the remaining hydrogen molecules are bound to the metal atom. The absorption energy for the first hydrogen was found to have a larger value for the Rh-doped BN sheet, whereas for the second and third hydrogen molecules, the absorption energies were higher for the Ni doped BN sheets. Upon addition of a fourth hydrogen molecule to the Ni doped BN sheets, the fourth hydrogen molecule moved to a distance of 3.855 Å. In the case of Rh-doped BN sheet, the Rh atom detached and acted in a similar way to a cluster. Thus Ni atoms are more stable on BN sheets, and have higher absorption energy compared to the Rh doped BN sheets (Venkataramanan et al. 2009).

Metallized graphene can be a potential high-capacity hydrogen storage medium. Graphene is metallized through charge donation by adsorbed Li atoms to its π^* -bands. Each positively charged Li ion can bind up to four H_2 by polarizing these molecules. The storage capacity up to the gravimetric density of 12.8 wt % is possible with a favorable average H_2 binding energy of 0.21 eV (Ataca et al. 2008).



■ Fig. 27-28

Plots of the spin density and electron density for the α -spin (up) and β -spin (down) states in nanoscale graphene. For the spin density, different colors indicate the α - and β -states, while for the electron density distribution (α - and β -states) the different colors correspond to different signs of the molecular orbital lobes. (a) The electron density distribution in pure graphene. (b) The electron density distribution for graphene with adsorbed water (Reprinted with permission from Berashevich and Chakraborty (2009). © (2009) by the American Physical Society)

Water and gas molecules adsorbed on nanoscale graphene play the role of defects which facilitate the tunability of the bandgap and allow one to control the magnetic ordering of localized states at the edges (Berashevich and Chakraborty 2009). The adsorbed molecules push the α -spin (up) and β -spin (down) states of graphene to the opposite (zigzag) edges such that the α - and β -spin states are localized at different zigzag edges. This breaks the symmetry that results in the opening of a large gap. The efficiency of the wavefunction displacement depends strongly on the type of molecules adsorbed on graphene (Berashevich and Chakraborty 2009). The influence of adsorption of water on the electronic and magnetic properties of graphene is based on calculation of the spin-polarized density functional theory and the results of the calculations are depicted in ► Fig. 27-28.

References

- Amorim, R. G., Fazzio, A., Antonelli, A., Novaes, F. D., & da Silva, A. J. R. (2007). Divacancies in graphene and carbon nanotubes. *Nano Letters*, 7, 2459.
- Anagnostatos, G. S. (1987). Magic numbers in small clusters of rare-gas and alkali atoms. *Physics Letters A*, 124, 85.
- Andzelm, J., Govind, N., & Maiti, A. (2006). Nanotube-based gas sensors — Role of structural defects. *Chemical Physics Letters*, 421, 58.
- Arantes, J. T., & Fazzio, A. (2007). Theoretical investigations of Ge nanowires grown along the [110] and [111] directions. *Nanotechnology*, 18, 295706.

- Areshkin, D. A., Gunlycke, D., & White, C. T. (2007). Ballistic transport in graphene nanostrips in the presence of disorder: importance of edge effects. *Nano Letters*, 7, 204.
- Ataca, C., Akturk, E., Ciraci, S., & Ustunel, H. (2008). High-capacity hydrogen storage by metallized graphene. *Applied Physics Letters*, 93, 043123.
- Balasubramanian, K. (1990). Spectroscopic constants and potential-energy curves of heavy p-block dimers and trimers. *Chemical Reviews*, 90, 93.
- Baletto, F., & Ferrando, R. (2005). Structural properties of nanoclusters: energetic, thermodynamic, and kinetic effects. *Reviews of Modern Physics*, 77, 371.
- Barone, V., Hod, O., & Scuseria, G. E. (2006). Electronic structure and stability of semiconducting graphene nanoribbons. *Nano Letters*, 6, 2748.
- Barreteau, C., Desjonqueres, M. C., & Spanjaard, D. (2000). Theoretical study of the icosahedral to cuboctahedral structural transition in Rh and Pd clusters. *European Physical Journal D*, 11, 395.
- Barth, S., Harnagea, C., Mathur, S., & Rosei, F. (2009). The elastic moduli of oriented tin oxide nanowires. *Nanotechnology*, 20, 115705.
- Baumeier, B., Kruger, P., & Pollmann, J. (2007). Structural, elastic, and electronic properties of SiC, BN, and BeO nanotubes. *Physical Review B*, 76, 085407.
- Berashevich, J., & Chakraborty, T. (2009). Tunable bandgap and magnetic ordering by adsorption of molecules on graphene. *Physical Review B*, 80, 033404.
- Bonacic-Koutecky, V., Fantucci, P., & Koutecky, J. (1991). Quantum chemistry of small clusters of elements of Groups Ia, Ib, and IIa: fundamental concepts, predictions, and interpretation of experiments. *Chemical Reviews*, 91, 1035.
- Botello-Mendez, A. R., Martinez-Martinez, M. T., Lopez-Urias, F., Terrones, M., & Terrones, H. (2007). Metallic edges in zinc oxide nanoribbons. *Chemical Physics Letters*, 448, 258.
- Brack, M. (1993). The physics of simple metal clusters: self-consistent jellium model and semiclassical approaches. *Reviews of Modern Physics*, 65, 677.
- Brenner, D. (1989). Relationship between the embedded-atom method and Tersoff potentials. *Physical Review Letters*, 63, 1022.
- Briere, T. M., Sluiter, M. H., Kumar, V., & Kawazoe, Y. (2002). Atomic structures and magnetic behavior of Mn clusters. *Physical Review B*, 66, 064412.
- Bromley, S. T., & Flikkema, E. (2005). Columnar-to-disk structural transition in nanoscale (SiO₂)_N Clusters. *Physical Review Letters*, 95, 185505.
- Bruno, M., Palumbo, M., Ossicini, S., & del Sole, E. (2007). First-principles optical properties of silicon and germanium nanowires. *Surface Science*, 601, 2707.
- Bulusu, S., Yoo, S., & Zeng, X. C. (2005). Search for global minimum geometries for medium sized germanium clusters: Ge₁₂-Ge₂₀. *Journal of Chemical Physics*, 122, 164305.
- Chan, T.-L., Ciobanu, C. V., Chuang, F.-C., Lu, N., Wang, C.-Z., & Ho, K.-M. (2006). Magic structures of H-Passivated (110) silicon nanowires. *Nano Letters*, 6, 277.
- Chen, Y. P., Xie, Y. E., & Yan, X. H. (2008). Electron transport of L-shaped graphene nanoribbons. *Journal of Applied Physics*, 103, 063711.
- Chopra, N. G., Luyken, R. J., Cherrey, K., Crespi, V. H., Cohen, M. L., Louie, S. G., & Zettl, A. (1995). Boron-nitride nanotubes. *Science*, 269, 966.
- Corso, M., Auwarter, W., Muntwiler, M., Tamai, A., Greber, T., & Osterwalder, J. (2004). Boron nitride nanomesh. *Science*, 303, 217.
- Darby, S., Mortimer-Jones, T. V., Johnston, R. L., & Roberts, C. (2002). Theoretical study of Cu-Au nanoalloy clusters using a genetic algorithm. *Journal of Chemical Physics*, 116, 1536.
- de Heer, W. A. (1993). The physics of simple metal clusters: experimental aspects and simple models. *Reviews of Modern Physics*, 65, 611.
- de Oliveira, I. S. S., & Miwa, R. H. (2009). Boron and nitrogen impurities in SiC nanowires. *Physical Review B*, 79, 085427.
- Doye, J. P. K. (2003). Identifying structural patterns in disordered metal clusters. *Physical Review B*, 68, 195418.
- Doye, J. P. K. (2006). Lead clusters: Different potentials, different structures. *Computational Materials Science*, 35, 227.
- Doye, J. P. K., & Wales, D. J. (1999). Structural transitions and global minima of sodium chloride clusters. *Physical Review B*, 59, 2292.
- Du, J., Shen, N., Zhu, L., & Wang, J. (2010). Emergence of noncollinear magnetic ordering in bimetallic Co_{6-n}Mn_n clusters. *Journal of Physics D*, 43, 015006.
- Dugan, N., & Erkoc, S. (2008). Stability analysis of graphene nanoribbons by molecular dynamics simulations. *Physica Status Solidi (B)*, 245, 695.
- Dugan, N., & Erkoc, S. (2009). Genetic algorithms in aication to the geometry optimization of nanoparticles. *Algorithms*, 2, 410.
- Enoki, T., & Takai, K. (2009). The edge state of nanographene and the magnetism of the

- edge-state spins. *Solid State Communications*, 149, 1144.
- Enyashin, A. N., & Seifert, G. (2005). Structure, stability and electronic properties of TiO₂ nanostructures. *Physica Status Solidi (B)*, 242, 1361.
- Erkoc, S. (1997). Empirical many-body potential energy function used in computer simulations Of condensed matter properties. *Physics Reports*, 278, 79.
- Erkoc, S. (2001). Empirical potential energy functions used in the simulations of materials properties. In D. Stauffer (Ed.), *Annual review of computational physics* (Vol. IX, pp. 1–103). Singapore: World Scientific.
- Erkoc, S. (2001). Structural and electronic properties of single-wall BN nanotubes. *Journal of Molecular Structure (THEOCHEM)*, 542, 89.
- Erkoc, S. (2003). Structural and electronic properties of “benzorods”. *Journal of Molecular Structure (THEOCHEM)*, 639, 157.
- Erkoc, S. (2004). Does tubular structure of carbon form only from graphine sheet? *Physica E*, 25, 69.
- Erkoc, S. (2004). Semi-empirical SCF-MO calculations for the structural and electronic properties of single-wall InP nanotubes. *Journal of Molecular Structure (THEOCHEM)*, 676, 109.
- Erkoc, S., & Kokten, H. (2005). Structural and electronic properties of single-wall ZnO nanotubes. *Physica E*, 28, 162.
- Erkoc, S., Malcioglu, O. B., & Tasci, E. (2004). Structural and electronic properties of single-wall GaN nanotubes: semi-empirical SCF-MO calculations. *Journal of Molecular Structure (THEOCHEM)*, 674, 1.
- Ezawa, M. (2006). Peculiar width dependence of the electronic properties of carbon nanoribbons. *Physical Review B*, 73, 045432.
- Fa, W., Luo, C., & Dong, J. (2005). Structure-dependent ferroelectricity of niobium clusters (Nb_N, N = 2 – 52). *Physical Review B*, 71, 245415.
- Fa, W., Luo, C., & Dong, J. (2006). Coexistence of ferroelectricity and ferromagnetism in tantalum clusters. *Journal of Chemical Physics*, 125, 114305.
- Finnis, M. W., & Sinclair, J. E. (1984). A simple empirical n-body potential for transition metals. *Philosophical Magazine A*, 50, 45.
- Freitag, M. (2008). Nanoelectronics goes flat out. *Nature Nanotechnology*, 3, 455.
- Gafner, Y. Y., Gafner, S. L., & Entel, P. (2004). Formation of an icosahedral structure during crystallization of nickel nanoclusters. *Physical Solid State*, 46, 1327.
- Gao, G., & Kang, H. S. (2008). First-principles study of silicon nitride nanotubes. *Physical Review B*, 78, 165425.
- Geim, A. K., & Novoselov, K. S. (2007). The rise of graphene. *Nature Materials*, 6, 183.
- Ghosh, P., Kahaly, M. U., & Waghmare, U. V. (2007). Atomic and electronic structures, elastic properties, and optical conductivity of bulk Te and Te nanowires: a first-principles study. *Physical Review B*, 75, 245437.
- Gorjizadeh, N., Farajian, A. A., Esfarjani, K., & Kawazoe, Y. (2008). Spin and band-gap engineering in doped graphene nanoribbons. *Physical Review B*, 78, 155427.
- Gunlycke, D., Li, J., Mintmire, J. W., & White, C. T. (2007). Altering low-bias transport in zigzag-edge graphene nanostrips with edge chemistry. *Applied Physics Letters*, 91, 112108.
- Haberland, H. (1994). *Clusters of atoms and molecules*. Berlin: Springer.
- Halicioglu, T., & Bauschlicher, C. W. (1988). Physics of microclusters. *Reports on Progress in Physics*, 51, 883.
- Han, M. Y., Ozyilmaz, B., Zhang, Y. B., & Kim, P. (2007). Energy band-gap engineering of graphene nanoribbons. *Physical Review Letters*, 98, 206805.
- Hartke, B. (2002). Structural transitions in clusters. *Angewandte Chemie (International Ed. in English)*, 41, 1468.
- Hestenes, M. R., & Stiefel, E. (1952). Methods of conjugate gradients for solving linear systems. *Journal of research of the National Bureau of Standards*, 49, 409.
- Hsu, P. J., & Lai, S. K. (2006). Structures of bimetallic clusters. *Journal of Chemical Physics*, 124, 044711.
- Hu, J., Liu, X. W., & Pan, B. C. (2008). A study of the size-dependent elastic properties of ZnO nanowires and nanotubes. *Nanotechnology*, 19, 285710.
- Huda, M. N., & Kleinman, L. (2006). h-BN monolayer adsorption on the Ni(111) surface: a density functional study. *Physical Review B*, 74, 075418.
- Jarrold, M. F. & Constant, V. A. (1991). Silicon cluster ions: evidence for a structural transition. *Physical Review Letters*, 67, 2994.
- Jayasekera, T., & Mintmire, J. W. (2007). Transport in multiterminal graphene nanodevices. *Nanotechnology*, 18, 424033.
- Jensen, P. J., & Pastor, G. M. (2003). Low-energy properties of two-dimensional magnetic nanostructures: interparticle interactions and disorder effects. *New Journal of Physics*, 5, 68.
- Jia, X., Hofmann, M., Meunier, V., Sumpter, B. G., Campos-Delgado, J., Romo-Herrera, J. M., Son, H.,

- Hsieh, Y.-P., Reina, A., Kong, J., Terrones, M., & Dresselhaus, M. S. (2009). Controlled formation of Sharp Zigzag and Armchair Edges in Graphitic Nanoribbons. *Science*, 323, 1701.
- Johnston, R. L. (2002). *Atomic and molecular clusters*. London: Taylor & Francis.
- Kabir, M., Mookerjee, A., & Kanhere, D. G. (2006). Structure, electronic properties, and magnetic transition in manganese clusters. *Physical Review B*, 73, 224439.
- Kagimura, R., Nunes, R. W., & Chacham, H. (2007). Surface dangling-bond states and band Line-ups in Hydrogen-Terminated Si, Ge, and Ge/Si nanowires. *Physical Review Letters*, 98, 026801.
- Kirkpatrick, S., Gelatt, C. D., & Vecchi, M. P. (1983). Optimization by simulated annealing. *Science*, 220, 671.
- Knickelbein, M. B. (2001). Experimental observation of superparamagnetism in manganese clusters. *Physical Review Letters*, 86, 5255.
- Kohler, C., Seifer, G., & Fraueheim, T. (2006). Magnetism and the potential energy hypersurfaces of Fe₅₃ to Fe₅₇. *Computational Materials Science*, 35, 297.
- Krainyukova, N. V. (2006). The crystal structure problem in noble gas nanoclusters. *Thin Solid Films*, 515, 1658.
- Kulkarni, A. J., Zhou, M., & Ke, F. J. (2005). Orientation and size dependence of the elastic properties of zinc oxide nanobelts. *Nanotechnology*, 16, 2749.
- Kumar, V., & Kawazoe, Y. (2002). Icosahedral growth, magnetic behavior, and adsorbate-induced metal-nonmetal transition in palladium clusters. *Physical Review B*, 66, 144413.
- Landau, L. D., & Lifshitz, E. M. (1980). *Statistical physics, Part I, sections 137 and 138*. Oxford: Pergamon.
- Lau, K. C., Pati, R., Pandey, R., & Pineda, A. C. (2006). First-principles study of the stability and electronic properties of sheets and nanotubes of elemental boron. *Chemical Physics Letters*, 418, 549.
- Lee, B., & Rudd, R. E. (2007). First-principles calculation of mechanical properties of Si<001> nanowires and comparison to nanomechanical theory. *Physical Review B*, 75, 195328.
- Lennard-Jones, J. E. (1931). Cohesion. *Proceedings of the Physical Society*, 43, 461.
- Li, F., Zhu, Z., Zhao, M., & Xia, Y. (2008a). Ab initio calculations on the magnetic properties of hydrogenated boron nitride nanotubes. *Journal of Physical Chemistry C*, 112, 16231.
- Li, Z. Q., Henriksen, E. A., Jiang, Z., Hao, Z., Martin, M. C., Kim, P., Stormer, H. L., & Basov, D. N. (2008b). Dirac charge dynamics in graphene by infrared spectroscopy. *Nature Physics*, 4, 532.
- Liang, H., & Upmanyu, M. (2006). Axial-strain-induced torsion in single-walled carbon nanotubes. *Physical Review Letters*, 96, 165501.
- Lin, Y.-M., Jenkins, K. A., Valdes-Garcia, A., Small, J. P., Farmer, D. B., & Avouris, P. (2009). Operation of graphene transistors at gigahertz frequencies. *Nano Letters*, 9, 422.
- Liu, J. F., Wright, A. R., Zhang, C., & Ma, Z. S. (2008). Strong terahertz conductance of graphene nanoribbons under a magnetic field. *A Physical Letters*, 93, 041106.
- Liu, X., Bauer, M., Bertagnolli, H., Roduner, E., van Slagere, J., & Philli F. (2006). Structure and magnetization of small monodisperse platinum clusters. *Physical Review Letters*, 97, 253401.
- Ma, S., & Wang, G. (2006). Structures of medium size germanium clusters. *Journal of Molecular Structure (THEOCHEM)*, 767, 75.
- Mackay, A. L. (1962). A dense non-crystallographic packing of equal spheres. *Acta Crystallographica*, 15, 916.
- Maiti, A. (2008). Multiscale modeling with carbon nanotubes. *Microelectronics Journal*, 39, 208.
- Malcioglu, O. B., & Erkoc, S. (2004). Stability of C₆₀ chains: Molecular Dynamics Simulations. *Journal of Molecular Graphics and Modelling*, 23, 367.
- Martin, T. P. (1996). Shells of atom. *Physics Reports*, 273, 199.
- Mermin, N. D. (1968). Crystalline order in two dimensions. *Physical Review*, 176, 250.
- Meyer, J. C., Geim, A. K., Katsnelson, M. I., Novoselov, K. S., Booth, T. J., & Roth, S. (2007). The structure of suspended graphene sheets. *Nature*, 446, 60.
- Michaelian, K., Rendon, N., & Garzon, I. L. (1999). Structure and energetics of Ni, Ag, and Au nanoclusters. *Physical Review B*, 60, 2000.
- Migas, D. B., & Borisenko, V. E. (2008). Effects of oxygen, fluorine, and hydroxyl passivation on electronic properties of (001)-oriented silicon nanowires. *Journal of Applied Physics*, 104, 024314.
- Moraga, G. G. (1993). *Cluster chemistry*. Berlin: Springer
- Morse, M. D. (1986). Clusters of transition-metal atoms. *Chemical Reviews*, 86, 1049.
- Nakabayashi, J., Yamamoto, D., & Kurihara, S. (2009). Band-selective filter in a zigzag graphene nanoribbon. *Physical Review Letters*, 102, 066803.
- Nava, P., Seierka, M., & Ahlrichs, R. (2003). Density functional study of palladium clusters. *Physical Chemistry Chemical Physics*, 5, 3372.

- Neto, A. H. C., Guinea, F., Peres, N. M. R., Novoselov, K. S., & Geim, A. K. (2009). The electronic properties of graphene. *Reviews of Modern Physics*, *81*, 109.
- Novoselov, K. S., Geim, A. K., Morozov, S. V., Jiang, D., Zhang, Y., Dubonos, S. V., Grigorieva, I. V., & Firsov, A. A. (2004). Electric field effect in atomically thin carbon films. *Science*, *306*, 666.
- Noya, E. G., & Doye, J. P. K. (2006). Structural transitions in the 309-atom magic number Lennard-Jones cluster. *Journal of Physical Chemistry*, *124*, 104503.
- Pan, Z. W., Dai, Z. R., & Wang, Z. L. (2001). Nanobelts of semiconducting oxides. *Science*, *291*, 1947.
- Pathak, S., Shenoy, V. B., & Baskaran, G. (2008). Possibility of High Tc Superconductivity in doped Graphene, arXiv:0809.0244v1 [cond-mat.suprcon] 1 Sep 2008.
- Pawluk, T., Hirata, Y., & Wang, L. (2005). Studies of iridium nanoparticles using density functional theory calculations. *Journal of Physical Chemistry B*, *109*, 20817.
- Payne, F. W., Jiang, W., & Bloomfield, L. A. (2006). Magnetism and magnetic isomers in free chromium clusters. *Physical Review Letters*, *97*, 193401.
- Pedersen, T. G., Flindt, C., Pedersen, J., Jauho, A.-P., Mortensen, N. A., & Pedersen, K. (2008). Optical properties of graphene antidot lattices. *Physical Review B*, *77*, 245431.
- Pedersen, T. G., Flindt, C., Pedersen, J., Mortensen, N. A., Jauho, A.-P., & Pedersen, K. (2008). Graphene antidot lattices: Designed defects and spin qubits. *Physical Review Letters*, *100*, 136804.
- Pekoz, R., & Erkoc, S. (2008). Quantum chemical treatment of Li/Li⁺ doped defected carbon nanocapsules. *Physica E*, *40*, 2752.
- Peres, N., Castro, A., & Guinea, F. (2006). Conductance quantization in mesoscopic graphene. *Physical Review B*, *73*, 195411.
- Peres, N. M. R., Guinea, F., & Neto, A. H. C. (2006). Electronic properties of two-dimensional carbon. *Annals of Physics*, *321*, 1559.
- Pisani, L., Chan, J. A., Montanari, B., & Harrison, N. M. (2007). Electronic structure and magnetic properties of graphitic ribbons. *Physical Review B*, *75*, 064418.
- Qi, J., Shi, D., Zhao, J., & Jiang, X. (2008). Stable structures and electronic properties of the oriented Bi Nanowires and Nanotubes from first-principle calculations. *Journal of Physical Chemistry C*, *112*, 10745.
- Rathi, S. J., & Ray, A. K. (2008). On the existence and stability of single walled SiGe nanotubes. *Chemical Physics Letters*, *466*, 79.
- Rey, C., Gallego, L. J., Garcia-Rodeja, J., Alonso, J. A., & Iniguez, M. P. (1993). Molecular-dynamics study of the binding energy and melting of transition-metal clusters. *Physical Review B*, *48*, 8253.
- Rodriguez-Lopez, J. L., Aguilera-Granja, F., Michaelian, K., & Vega, A. (2003). Structure and magnetism of cobalt clusters. *Physical Review B*, *67*, 174413.
- Rosales, L., Pacheco, M., Barticevic, Z., Latge, A., & Orellana, P. A. (2008). Transport properties of graphene nanoribbons with side-attached organic molecules. *Nanotechnology*, *19*, 065402.
- Rudd, R. E., & Lee, B. (2008). Mechanics of silicon nanowires: size-dependent elasticity from first principles. *Molecular Simulation*, *34*, 1.
- Rurali, R. (2005). Electronic and structural properties of silicon carbide nanowires. *Physical Review B*, *71*, 205405.
- Rurali, R., & Lorente, N. (2005). Metallic and semimetallic silicon (100) nanowires. *Physical Review Letters*, *94*, 026805.
- Sadowski, T., & Ramprasad, R. (2007). Stability and electronic structure of CdSe nanorods from first principles. *Physical Review B*, *76*, 235310.
- Sasaki, K. I., Murakami, S., & Saito, R. (2006). Gauge field for edge state in graphene. *Journal of the Physical Society of Japan*, *75*, 074713.
- Sevincli, H., Topsakal, M., Durgun, E., & Ciraci, S. (2008). Electronic and magnetic properties of 3d transition-metal atom adsorbed graphene and graphene nanoribbons. *Physical Review B*, *77*, 195434.
- Shevlin, S. A., & Guo, Z. X. (2006). Transition-metal-doping-enhanced hydrogen storage in boron nitride systems. *Applied Physics Letters*, *89*, 153104.
- Shvartsburg, A. A., & Jarrold, M. F. (1999). Tin clusters adopt prolate geometries. *Physical Review A*, *60*, 1235.
- Shvartsburg, A. A., & Jarrold, M. F. (2000). Transition from covalent to metallic behavior in group-14 clusters. *Chemical Physics Letters*, *317*, 615.
- Sieck, A., Frauenheim, T., & Jackson, K. A. (2003). Shape transition of medium-sized neutral silicon clusters. *Physica Status Solidi B*, *240*, 537.
- Singh, R., & Kroll, P. (2009). Magnetism in graphene due to single-atom defects: dependence on the concentration and packing geometry of defects. *Journal of Physics: Condensed Matter*, *21*, 196002.
- Son, Y. W., Cohen, M. L., & Louie, S. G. (2006). Half-metallic graphene nanoribbons. *Nature*, *444*, 347.
- Stillinger, F. H., & Weber, T. A. (1985). Computer simulation of local order in condensed phases of silicon. *Physical Review B*, *31*, 5262.

- Sun, X. H., Li, C. P., Wong, W. K., Wong, N. B., Lee, C. S., Lee, S. T., & Teo, B. K. (2002). Formation of silicon carbide nanotubes and nanowires via reaction of silicon (from disproportionation of silicon monoxide) with carbon nanotubes. *Journal of the American Chemical Society*, *124*, 14464.
- Tang, C., Yan, W., Zheng, Y., Li, G., & Li, L. (2008). Dirac equation description on the electronic states and magnetic properties of a square graphene quantum dot, arXiv:0811.4312v1 [cond-mat.str-el] 26 Nov 2008.
- Tiago, M. L., Zhou, Y., Alemany, M. M. G., Saad, Y., & Chelikowski, J. R. (2006). Evolution of magnetism in iron from the atom to the bulk. *Physical Review Letters*, *97*, 147201.
- Topsakal, M., Akturk, E., Sevincli, H., and Ciraci, S. (2008). First-principles approach to monitoring the band gap and magnetic state of a graphene nanoribbon via its vacancies. *Physical Review B*, *78*, 235435.
- Ustunel, H., & Erkoc, S. (2007). Structural properties and stability of nanoclusters. *Journal of Computational and Theoretical Nanoscience*, *4*, 928.
- Ustunel, H., Roundy, D., & Arias, T. A. (2005). Modelling a suspended nanotube oscillator. *Nano Letters*, *5*, 523.
- Venkataramanan, N. J., Khazaei, M., Sahara, R., Mizuseki, H., & Kawazoe, Y. (2009). First-principles study of hydrogen storage over Ni and Rh doped BN sheets. *Chemical Physics*, *359*, 173.
- Vvedensky, D. D. (2004). Multiscale modelling of nanostructures. *Journal of Physics: Condensed Matter*, *16*, R1537.
- Wales, D. J. & Doye, J. P. K. (1997). Global optimization by basin-hopping and the lowest energy structures of Lennard-Jones clusters containing up to 110 atoms. *Journal of Physical Chemistry A*, *101*, 5111.
- Wang, G., & Li, X. (2008). Predicting Young's modulus of nanowires from first-principles calculations on their surface and bulk materials. *Journal of Applied Physics*, *104*, 113517.
- Wang, W. L., Meng, S., & Kaxiras, E. (2008). Graphene nanoflakes with large spin. *Nano Letters*, *8*, 241.
- Wang, Z. F., Li, Q., Zheng, H., Ren, H., Su, H., Shi, Q. W., & Chen, J. (2007). Tuning the electronic structure of graphene nanoribbons through chemical edge modification: a theoretical study. *Physical Review B*, *75*, 113406.
- Wang, Z. L. (2004). Functional oxide nanobelts: materials, properties and potential applications in nanosystems and biotechnology. *Annual Review of Physical Chemistry*, *55*, 159.
- Weltner, W. J., & Van Zee, R. J. (1984). Transition metal molecules. *Annual Review of Physical Chemistry*, *35*, 291.
- Wright, A. R., Wang, G. X., Xu, W., Zeng, Z., & Zhang, C. (2009). The spin-orbit interaction enhanced terahertz absorption in graphene around the K point. *Microelectronics Journal*, *40*, 857.
- Wu, K. L., Lai, S. K., & Lin, S. D. (2005). Finite temperature properties for zinc nanoclusters. *Molecular Simulation*, *31*, 399.
- Wu, X., & Zeng, X. C. (2008). Sawtooth-like graphene nanoribbon. *Nano Research*, *1*, 40.
- Wu, X., Pei, Y., & Zeng, X. C. (2009). B₂C graphene, nanotubes, and nanoribbons. *Nano Letters*. doi: 10.1021/nl803758s.
- Xie, Y. E., Chen, Y. P., Sun, L. Z., Zhang, K. W., & Zhong, J. X. (2009). The effect of corner form on electron transport of L-shaped graphene nanoribbons. *Physica B*, *404*, 1771.
- Yang, M., Jackson, K. A., Koehler, C., Frauenheim, T., & Jellinek, J. (2006). Structure and shape variations in intermediate-size cor clusters. *Journal of Chemical Physics*, *124*, 024308.
- Yang, R., & Wang, Z. L. (2006). Springs, rings, and spirals of rutile-structured tin oxide nanobelts. *Journal of the American Chemical Society*, *128*, 1466.
- Yao, Y. H., Gu, X., Ji, M., Gong, X. G., & Wang, D.-S. (2007). Structures and magnetic moments of Ni_n ($n = 10 - 60$) clusters. *Physics Letters A*, *360*, 629.
- Zhang, C., Chen, L., & Ma, Z. S. (2008). Orientation dependence of the optical spectra in graphene at high frequencies. *Physical Review B*, *77*, 241402.
- Zhang, W., Ran, X., Zhao, H., & Wang, L. (2004). The nonmetallicity of molybdenum clusters. *Journal of Chemical Physics*, *121*, 7717.
- Zhang, X. W., & Yang, G. W. (2009). Novel band structures and transport properties from graphene nanoribbons with armchair edges. *Journal of Physical Chemistry C*, *113*, 4662.
- Zhang, Y. Y., Wang, C. M., & Tan, V. B. C. (2008). Examining the effects of wall numbers on buckling behavior and mechanical properties of multiwalled carbon nanotubes via molecular dynamics simulations. *Journal of Applied Physics*, *103*, 053505.
- Zhou, J., & Dong, J. (2008). Radial breathing-like mode of wide carbon nanoribbon. *Physics Letters A*. doi: 10.1016/j.physleta.2008.10.059.

